



UNIVERSIDAD NACIONAL AUTÓNOMA DE MÉXICO  
POSGRADO EN CIENCIAS FÍSICAS

ELECTROMAGNETICALLY INDUCED TRANSPARENCY WITH RYDBERG  
STATES

TESIS  
QUE PARA OPTAR POR EL GRADO DE:  
MAESTRO EN FÍSICA

PRESENTA:  
EDUARDO ESQUIVEL RAMÍREZ

DIRECTOR DE TESIS  
DR. ASAF PARIS MANDOKI  
IF, UNAM

MIEMBROS DEL COMITÉ TUTOR  
JORGE AMIN SEMAN HARUTINIAN  
IF, UNAM  
PEDRO ANTONIO QUINTO SU  
ICN, UNAM

CIUDAD UNIVERSITARIA, CD.MX., OCTUBRE, 2022



Universidad Nacional  
Autónoma de México

Dirección General de Bibliotecas de la UNAM

**Biblioteca Central**



**UNAM – Dirección General de Bibliotecas**  
**Tesis Digitales**  
**Restricciones de uso**

**DERECHOS RESERVADOS ©**  
**PROHIBIDA SU REPRODUCCIÓN TOTAL O PARCIAL**

Todo el material contenido en esta tesis esta protegido por la Ley Federal del Derecho de Autor (LFDA) de los Estados Unidos Mexicanos (México).

El uso de imágenes, fragmentos de videos, y demás material que sea objeto de protección de los derechos de autor, será exclusivamente para fines educativos e informativos y deberá citar la fuente donde la obtuvo mencionando el autor o autores. Cualquier uso distinto como el lucro, reproducción, edición o modificación, será perseguido y sancionado por el respectivo titular de los Derechos de Autor.

## Hoja de datos del jurado

1. Datos del alumno  
Esquivel Ramírez Eduardo  
edy\_95fis@ciencias.unam.mx
2. Datos del tutor  
Dr. Asaf Paris Mandoki
3. Datos del sinodal 1  
Dr. Daniel Sahagún Sánchez
4. Datos del sinodal 2  
Dr. Pablo Barberis Blostein
5. Datos del sinodal 3  
Dr. José Ignacio Jiménez Mier y Terán
6. Datos del sinodal 4  
Dr. Arturo Camacho Guardian



---

---

# Agradecimientos

---

---

Todo el trabajo de mi vida será siempre dedicado a mis padres. Por su amor, apoyo y valores siempre estaré agradecido. Los amo.

A todas las personas que estuvieron cuando más las necesité: Jime, Rennie, Sofi, Yess, Ruthy, Val, Lariza, Dr. Giorgioro, Alis, Liz y Oli. Tengan presente que este trabajo es fruto de su cariño y el cuidado que me dieron durante meses. Los llevo siempre en mi pensamiento.

Invaluable ha sido la ayuda en este camino de mi camarada Uthhoff. Siempre dispuesto a ayudar y resolver cualquier contratiempo, es lo que un camarada haría. Gracias, camarada.

Todas esas discusiones interminables sobre temas varios no han tenido más que un impacto positivo en mi persona. Gracias por todo, Gio. Al mismo tiempo agradezco a Diego González por su apoyo con las imágenes para poder terminar mi trabajo y en general a todo el grupo de OCR por su disposición.

Es imperativo mencionar a un hombre al que he decidido seguir, mi tutor Asaf Paris Mandoki. No tengo forma de agradecerle a la vida haber llegado a tocar tu puerta para hacer mi servicio social. Eres mi capitán.

La manera en que el buceo ha transformado mi vida es increíble. El mar me ha regalado grandes maestros y hermanos: Bruno, Rogelio, Iván, gracias por todo lo que me han enseñado y ayudado. Por muchas inmersiones más.

Oportunidades de crear una comunidad tan cercana dentro de un área de trabajo son pocas, tengo la fortuna de decir que he encontrado una segunda familia en el HHH Club de la Comida Puerca, gracias a todos los miembros de este finísimo club por su cariño y apoyo en las locuras.

Especialmente quiero agradecer a Jimena que desde el segundo uno en que mis días se tornaron oscuros estuvo ahí día y noche para abrazarme y darme alientos. Tu cariño me tiene aquí hoy. Gracias por siempre.

Siempre tengo en mi pensamiento palabra y corazón a los suavimenes, siempre suaves nunca inmenes. Embrión y Jesucristo: la comedia jamás morirá.

También quiero mencionar a mi maestra de poesía Martha Mega, me permitió la entrada a un mundo que no conocía y veía muy lejano pero que ahora atesoro y jamás dejaré. La poesía también me mantuvo con los pies en la tierra durante momentos difíciles. Gracias por

---

tu sensibilidad y disposición para compartir tus tesoros, Martha.

Una de las personas más importantes en los últimos años para mi ha sido mi profesor de piano Raúl de la Mora a quien agradezco su empeño y facilidades que me ha brindado para que yo pueda seguir estudiando lo que tanto me apasiona.

Valiosas e irremplazables han sido las lecciones que me han dado mis maestros de natación, piano, física, poesía y buceo en la vida a todos ellos quiero agradecerles y decirles que su labor y esfuerzo durante tantos años se ha visto reflejado en mi y en este trabajo.

Oso, te nos adelantaste en el camino. Siempre te llevaré en mi mente con una sonrisa en el rostro pues así es como siempre fuiste conmigo. No tuve la oportunidad de despedirme de ti pero te dedico esta obra. Un abrazo grande donde quiera que estes y gracias por tanto que me diste. Descansa en paz.

Agradezco a Carlos Gardea por desarrollar gran parte de la instrumentación del proyecto y a Rodrigo Gutiérrez por sus numerosas asesorías técnicas.

Quiero agradecer también al proyecto: DAPA-UNAM, PAPIIT:IA104220.

Un agradecimiento al proyecto: Coordinación de la Investigación Científica UNAM: LANMAC-2020, LANMAC-2021, LANMAC-2022.

Ineludiblemente quiero finalizar agradeciendo a los proyectos CONACYT:  
-Investigación Científica Básica A1-S-29630  
-Laboratorio Nacional: 299057,314860, 315938.

---

---

# Contents

---

---

<b>Abstract</b>	<b>1</b>
<b>Introduction</b>	<b>3</b>
<b>1 Atom-light interaction</b>	<b>5</b>
1.1 Three level atom . . . . .	5
1.1.1 Hamiltonian . . . . .	5
1.1.2 Master Equation . . . . .	8
1.1.3 Electric susceptibility . . . . .	8
1.2 Electromagnetically induced transparency . . . . .	9
1.2.1 Dressed-state picture and dark state . . . . .	10
1.2.2 Optical response . . . . .	11
1.2.3 Hyperfine structure . . . . .	13
<b>2 Rubidium</b>	<b>17</b>
2.1 Electronic configuration . . . . .	17
2.1.1 D2 transition . . . . .	19
2.2 Rydberg states . . . . .	21
2.2.1 Rydberg transitions . . . . .	22
2.2.2 Energy levels . . . . .	23
<b>3 Experimental setup</b>	<b>25</b>
3.1 Laser system . . . . .	25
3.1.1 Digital locking . . . . .	26
3.1.2 Beatlock rack module . . . . .	30
3.2 Magneto-optical trap . . . . .	31
3.2.1 Vacuum system . . . . .	31
3.2.2 Coils . . . . .	32
3.2.3 Optics . . . . .	33

---

3.3	EIT with Rydberg states . . . . .	33
3.3.1	Optics . . . . .	33
3.3.2	Sequence and data processing . . . . .	34
<b>4</b>	<b>Results</b>	<b>37</b>
4.1	EIT with Rydberg states . . . . .	37
4.1.1	Control frequency dependence . . . . .	39
4.1.2	Power dependence . . . . .	40
4.1.3	Polarization dependence . . . . .	42
<b>5</b>	<b>Conclusions and perspectives</b>	<b>43</b>
5.1	Conclusions . . . . .	43
5.2	Optical pumping and magnetic compensation fields . . . . .	44
5.3	Sub-Doppler cooling . . . . .	44
5.4	Observation of quantum nonlinearities . . . . .	45



---

---

# List of Tables

---

---

2.1	Relevant characteristics of isotopes $^{85}\text{Rb}$ and $^{87}\text{Rb}$ . . . . .	18
-----	--	----



---



---

# List of Figures

---



---

1.1	Energy levels and detunings of the three level atom in the ladder configuration, $\Gamma_1$ and $\Gamma_2$ are the decay rates from excited states. . . . .	6
1.2	Imaginary and real parts of the three level atom electric susceptibility as function of $\delta_1$ . . . . .	10
1.3	Absorption profile of the three level atom under electromagnetically induced transparency ( $\delta_2 = 0$ ) with the control beam on (blue) and off (orange). . . . .	13
1.4	Convolution between the absorption profile of the three level atom under EIT and different Gaussian profiles. The full width half maximum of the Gaussian functions is $2.35\sigma$ . The dotted line is the original EIT profile. . . . .	13
2.1	Measured saturated absorption spectroscopy of line D2 of $^{85}\text{Rb}$ and $^{87}\text{Rb}$ . . . . .	18
2.2	The transition matrix elements for $F = 2 \rightarrow F' = 3$ in $^{87}\text{Rb}$ expressed as multiples of the reduced dipole matrix elements. . . . .	20
2.3	The transition matrix elements for $F = 3 \rightarrow F' = 4$ in $^{85}\text{Rb}$ expressed as multiples of the reduced dipole matrix elements. . . . .	21
2.4	Energy levels of the transitions to Rydberg states in rubidium. Rabi frequencies $\Omega_p$ and $\Omega_c$ characterizes the interaction strength between probe and control fields and the atoms. $\Omega_R$ is the Rabi frequency in the single photon transition scheme. . . . .	22
2.5	The transition matrix elements for $5^2P_{3/2} \rightarrow n^2S_{1/2}$ in $^{87}\text{Rb}$ expressed as multiples of the reduced dipole matrix element. . . . .	23
3.1	Schematic of the digital lock loop. A fraction of the light from primary and secondary lasers are combined on a non polarizing beam splitter (NPBS) to generate a beam measured on a photodiode. Signal is amplified and compared to a LO by the PLL to generate the error signal. FET and piezo-electric modulations are feeded back to the secondary laser controller to close the loop. . . . .	26

3.2	Schematic of the PFD functioning. The frequency divided signals of the beatnote and LO are fed into the clock channel of two flip flops. Whenever there is a rise in the clock channels, a high state is written to the Q outputs. They are then compared in the AND gate and whenever they are both equal the system is reset to a low state, otherwise the difference of the signals is delivered in the charge pump (CP) output as the error signal. . . . .	27
3.3	Signal processing circuit schematic. The circuit shifts, amplifies, clamps and divide the error signal to produce a slow and fast feedback. . . . .	29
3.4	FET modulation circuit schematic. A positive voltage causes the JFET to bleed a small amount of current away from the diode. . . . .	30
3.5	Beatnote error signal with FET modulation technique off (blue) and on (red). . .	30
3.6	Rack module of the beatlock locking system. (a) Rack module assembled. (b) Rack module board layout. . . . .	31
3.7	Photograph of the first $^{87}\text{Rb}$ MOT made in the Laboratorio de Óptica Cuántica de Rydberg on november 24 2021. . . . .	32
3.8	Coils built for the magneto-optical trap of $^{85}\text{Rb}$ and $^{87}\text{Rb}$ atoms. . . . .	32
3.9	Photo of the science chamber and the optical arrangement we use for the MOT.	33
3.10	Optical scheme for the generation of Rydberg states under EIT conditions. . . .	34
3.11	Experimental sequence used for the acquisition of data to detect EIT with Rydberg states in a $^{87}\text{Rb}$ MOT. The loading time of the MOT is 3 s. Time of flight 2.3 ms. The exposure time of the CCD is 200 $\mu\text{s}$ . . . . .	35
4.1	Transmittance profile of the atomic media as the probe beam is scanned around the $5S_{1/2} \rightarrow 5P_{3/2}$ transition with control beam off (blue dots) and control beam on (orange dots). To make the fit shown with a solid line we constrain the polarization purities between 0.9 and 1.0 for each beam, the optical density on resonance $OD_0 = 10$ as we can measure it when the control beam is off and we let the detuning $\delta_2$ as well as the intensities of the probe and control beam $I_p$ and $I_c$ as free parameters. Multiple windows of transparency arise due to the hyperfine structure of the $^{87}\text{Rb}$ atoms. Here we use a power of 1.46 $\mu\text{W}$ of the probe beam and 55 mW of control beam. . . . .	38

- 
- 4.2 Transmittance profile of the atomic media with two different values of control beam detuning  $\delta_2 = 0$  MHz (orange dots) and  $\delta_2 = -2$  MHz (green dots), base line for reference (blue dots), the fits are shown with solid lines. To make the shifted window fit we constrain the polarization purities between 0.9 and 1.0 for each beam, the optical density on resonance  $OD_0 = 10$  and we let the detuning  $\delta_2$  as well as the intensities of the probe and control beam  $I_p$  and  $I_c$  as free parameters resulting in  $\delta_2 = -1.5320$  MHz. The set of EIT windows moves together as the frequency of the control beam changes. Here we use a power of  $1.46 \mu\text{W}$  of the probe beam and  $55 \text{ mW}$  of control beam. . . . . 39
- 4.3 Transmittance profile of the atomic media for different control beam powers (dotted plots). The fits shown with solid lines were made fixing the polarization purities between 0.9 and 1.0 as well as the probe beam intensity with the value calculated by the program for the  $55 \text{ mW}$  measurement and leaving the magnetic field, detunings and control beam intensity as free parameters. The probe beam power was kept at  $1.46 \mu\text{W}$ . The jump downwards of the green graph corresponds with a point taken when control beam was unlocked from  $\delta_2 = 0$ . . . . . 40
- 4.4 Transmittance profile of the atomic media for different probe beam power outputs (dotted plots). The fits are shown with solid lines these were made fixing the polarization purities between 0.9 and 1.0 as well as the control beam intensity with the value calculated by the program for the  $1.56 \mu\text{W}$  measurement and leaving the magnetic field, detunings and probe beam intensity as free parameters. The control beam power was kept at  $70 \text{ mW}$ . . . . . 41
- 4.5 Transmittance profile of the atomic media as we rotate the control beam quarter-wave plate (dotted plots). We use  $1.46 \mu\text{W}$  of the probe beam and  $55 \text{ mW}$  of control beam for this measure. . . . . 42
- 5.1 Drawing of the magnetic field compensation coils for the Laboratorio de Óptica Cuántica de Rydberg experiment. . . . . 44



---

---

# Abstract

---

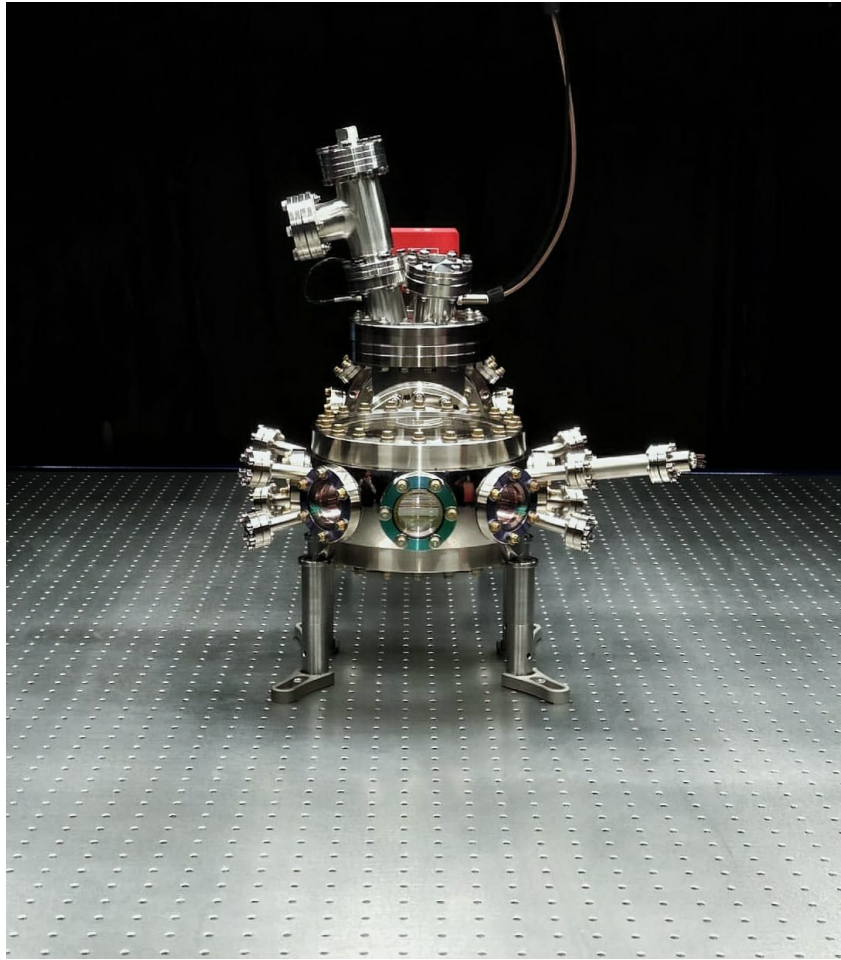
---

In this thesis we present the theoretical and experimental details about the detection of electromagnetically induced transparency (EIT) with Rydberg states in a cold sample of  $^{87}\text{Rb}$  atoms.

We present a semiclassical three level atom model of light matter interaction to explain the EIT phenomena and we extend it to include the hyperfine levels of real atoms to understand the multiple transmission windows we observe. We explain the relevant characteristics of rubidium in order to excite Rydberg levels. On the other hand we study the experimental details of the frequency locking system using an optical beatnote which paved the way for the construction of the magneto-optical trap that cools and traps atoms of  $^{85}\text{Rb}$  y  $^{87}\text{Rb}$  to temperatures of  $\sim 100\mu\text{K}$  in which we generate the Rydberg excitations and observe EIT.

En esta tesis se presentan los detalles teóricos y experimentales acerca de la medición de transparencias electromagnéticamente inducidas, EIT por sus siglas en inglés, con estados de Rydberg en una nube fría de átomos de  $^{87}\text{Rb}$ .

Se presenta un modelo semiclásico del átomo de tres niveles de interacción luz-materia para explicar el fenómeno de EIT y se extiende a un modelo que incluye la estructura hiperfina de los átomos para comprender las múltiples ventanas de transmisión observadas. Se explican las características relevantes del rubidio para excitar a estados de Rydberg. Así mismo se presentan los detalles experimentales del sistema de anclaje de láseres a partir de un batido de frecuencias que permitió la construcción de la trampa magneto-óptica, que permite enfriar átomos de  $^{85}\text{Rb}$  y  $^{87}\text{Rb}$  a temperaturas de  $\sim 100\mu\text{K}$ , misma en la que generamos excitaciones de Rydberg y observamos EIT.



Vacuum chamber for experiments of quantum optics at a few photon level using Rydberg atoms of the Laboratorio de Óptica Cuántica de Rydberg at Instituto de Física, UNAM.



---

---

# Introduction

---

---

The realization of an experiment in which we can achieve non-linear optical effects at a few photon level is of interest for the study of fundamental processes and for its technological applications. The interaction between photons allows the creation of non classical states of light, study the dynamics of manybody quantum systems [1] and the development of technologies for quantum information processing [2, 3, 4].

At a few photon level the optical nonlinearities arise when the the medium response to a second photon is different than to the first [5]. In classical optics the nonlinear regime is difficult to reach because great intensities of the fields are needed. To enhance the probability of observing nonlinear effects one can increase the amplitude of the optical fields or the interaction cross-section between the field and the receiver but the cross-section cannot be controlled in typical materials and the alternative is to increase the power of the light.

Various options exist to obtain a non linear optical response using few photons. For instance, the optical cavities of highfinesse where there is a single atom inside [6] or the use of optical nano-fibers with atoms trapped around them [7]. Another option, which is in the interest of this work, is the strong interaction between atoms in Rydberg states, these are atoms excited to a high principal quantum number  $n \geq 20$ . The properties of this atoms, like the half-life time of the states or polarizability, scale like powers of  $n$  and they are greatly enhanced compared with atoms in lower energy levels. Because of this, the Rydberg atoms exhibit a van der Waals interaction potential  $U(R) = C_6/R^6$  where  $R$  is the interatomic distance and  $C_6 \propto n^{11}$ . This potential provokes an energy shift on the quantum states of the atoms in a close neighborhood when a first Rydberg atom is created, if the shift is greater than the frequency linewidth of the excitation laser then the generation of a second Rydberg atom becomes impossible, this is a non-linear effect known as Rydberg blockade.

In the year 2001 Lukin *et al* proposed for the first time the use of the Rydberg blockade to generate quantum states of light [8]. Nevertheless, the experimental techniques didn't exist yet because almost everyone used destructive detection techniques, like ionization, and the coherent interaction of atom and light had not been observed. The key was electromagnetically induced transparency (EIT), the main focus of this work. In EIT a control field creates a transparency

window for resonant light with atoms in an otherwise opaque medium getting a non-destructive detection technique [9]. The first experiments that used EIT to detect Rydberg states with quantum numbers up to  $n = 124$  in a hot cell were reported by Mohapatra *et al* in 2007 [10], then Dudin and Kuzmich [11], Peyronel *et al* [12] and Maxwell [13] made the first experiments showing the manipulation of light at a few photon level.

In this thesis all the theoretical and experimental details that lead us to the detection of Rydberg states with a principal quantum number of  $n = 28$  in a cold sample of  $^{87}\text{Rb}$  atoms trapped in a magneto-optical trap using electromagnetically induced transparency are presented.

In the first chapter the theoretical models of atom-light interaction are explained, this allows us to understand what we observe in the experiment, here we derive the mathematical expression for EIT in a three level atom and an extension to hyperfine levels is shown. In the second chapter all the relevant physical properties of rubidium are reviewed, this is the atomic species we chose for the experiment. In the third chapter all the experimental details are contained, here we present the development of a frequency locking system using a beatnote of two different lasers which led us to the building of the locking system for the cooling, repumping and probing lasers. Moreover, we present the details of the optical scheme and the sequence used for EIT detection. In the fourth chapter the results and discussion are presented. Finally in chapter number five we present the conclusions and the perspectives of the near future work in the Laboratorio de Óptica Cuántica de Rydberg.

# Chapter 1

---

---

## Atom-light interaction

---

---

1.1	Three level atom . . . . .	5
1.1.1	Hamiltonian . . . . .	5
1.1.2	Master Equation . . . . .	8
1.1.3	Electric susceptibility . . . . .	8
1.2	Electromagnetically induced transparency . . . . .	9
1.2.1	Dressed-state picture and dark state . . . . .	10
1.2.2	Optical response . . . . .	11
1.2.3	Hyperfine structure . . . . .	13

In this chapter we describe the atom-light interaction model we will use as the basis for understanding all the physical phenomena we present in this work. First we will study the three level atom from the Hamiltonian of the system up to the electric susceptibility. Then we will use the latter to predict the behavior of this system in the laboratory. Finally we derive an expression for EIT in a real atom including hyperfine levels.

### 1.1 Three level atom

The two and three level atom have been studied in several configurations by a wide range of authors [14], I therefore present only a brief overview of the atom-light interaction theory relevant for our purposes.

#### 1.1.1 Hamiltonian

Consider the energy level structure of a three level atom in the ladder configuration as depicted in figure 1.1, we will label the ground state, the first excited state and the Rydberg state as

$|g\rangle$ ,  $|e\rangle$  and  $|r\rangle$  respectively, and we will denote the resonant frequencies between  $|g\rangle$  and  $|e\rangle$  as  $\omega_1$  and  $\omega_2$  between  $|e\rangle$  and  $|r\rangle$ . Here the ground and Rydberg states have parity opposite to the first excited state. In rubidium, as we will see in the next chapter, the ground state  $|g\rangle$  corresponds to the  $5S_{1/2}$  state,  $|e\rangle$  will be the  $5P_{3/2}$  state and the Rydberg level  $|r\rangle$  could be any  $nS$  or  $nD$  state with  $n \geq 20$ .

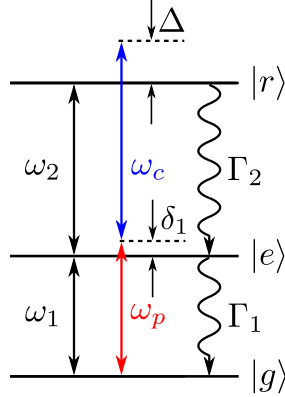


Figure 1.1: Energy levels and detunings of the three level atom in the ladder configuration,  $\Gamma_1$  and  $\Gamma_2$  are the decay rates from excited states.

The combined optical field has the form:

$$\mathbf{E}(\mathbf{r}, t) = \hat{\epsilon}_p E_p \cos(\mathbf{k}_p \cdot \mathbf{r} - \omega_p t) + \hat{\epsilon}_c E_c \cos(\mathbf{k}_c \cdot \mathbf{r} - \omega_c t), \quad (1.1)$$

we will call *probe beam* the field that oscillates with frequency  $\omega_p$  and polarization vector  $\hat{\epsilon}_p$  and *control beam* will be the field that oscillates with frequency  $\omega_c$  and polarization vector  $\hat{\epsilon}_c$ . In the dipole approximation and decomposing the field in the positive and negative frequencies we get:

$$\mathbf{E}(t) = \underbrace{\frac{1}{2} (\hat{\epsilon}_p E_p e^{-i\omega_p t} + \hat{\epsilon}_c E_c e^{-i\omega_c t})}_{\mathbf{E}^{(+)}(t)} + \underbrace{\frac{1}{2} (\hat{\epsilon}_p E_p e^{i\omega_p t} + \hat{\epsilon}_c E_c e^{i\omega_c t})}_{\mathbf{E}^{(-)}(t)}. \quad (1.2)$$

We will consider the detunings  $\delta_1 := \omega_p - \omega_1$  and  $\delta_2 := \omega_c - \omega_2$ , thus  $\Delta = \delta_1 + \delta_2$ . We assume that the fields  $E_p$  and  $E_c$  couple only  $|g\rangle$  to  $|e\rangle$  and  $|e\rangle$  to  $|r\rangle$  respectively as we will consider small detunings.

The atomic Hamiltonian of the three level atom is:

$$H_A = \hbar\omega_1 |e\rangle \langle e| + \hbar(\omega_1 + \omega_2) |r\rangle \langle r|, \quad (1.3)$$

also in the dipole approximation the atom-field interaction Hamiltonian is:

$$H_{int} = -\mathbf{d} \cdot \mathbf{E}, \quad (1.4)$$

where  $\mathbf{d}$  is the dipole operator. We can decompose this operator using the identity matrix  $\mathbb{1} = |g\rangle\langle g| + |e\rangle\langle e| + |r\rangle\langle r|$ :

$$\mathbf{d} = \underbrace{\langle g|\mathbf{d}|e\rangle\sigma_1 + \langle e|\mathbf{d}|r\rangle\sigma_2}_{\mathbf{d}^{(+)}} + \underbrace{\langle g|\mathbf{d}|e\rangle\sigma_1^\dagger + \langle e|\mathbf{d}|r\rangle\sigma_2^\dagger}_{\mathbf{d}^{(-)}}, \quad (1.5)$$

where  $\sigma_1 = |g\rangle\langle e|$  and  $\sigma_2 = |e\rangle\langle r|$  are the projection operators for this system. Using equation 1.5 we can write the interaction Hamiltonian in the rotating wave approximation (RWA) [14]:

$$H_{int} = -\mathbf{d}^{(+)} \cdot \mathbf{E}^{(-)} - \mathbf{d}^{(-)} \cdot \mathbf{E}^{(+)}. \quad (1.6)$$

Finally taking into consideration that  $\omega_2 \gg \omega_1$ ,  $\omega_1 \approx \omega_p$  and  $\omega_2 \approx \omega_c$  the Hamiltonian is:

$$H_{int} = \frac{\hbar\Omega_p}{2} \left( e^{i\omega_p t} \sigma_1 + e^{-i\omega_p t} \sigma_1^\dagger \right) + \frac{\hbar\Omega_c}{2} \left( e^{i\omega_c t} \sigma_2 + e^{-i\omega_c t} \sigma_2^\dagger \right), \quad (1.7)$$

where:

$$\Omega_p = -\frac{\langle g|\hat{\varepsilon}_p \cdot \mathbf{d}|e\rangle E_p}{\hbar} \quad \text{y} \quad \Omega_c = -\frac{\langle e|\hat{\varepsilon}_c \cdot \mathbf{d}|r\rangle E_c}{\hbar} \quad (1.8)$$

are the Rabi frequencies. Note that as we are not trying to describe coherent dynamics we are ignoring the phases between the Rabi frequencies. Then the full Hamiltonian  $H = H_A + H_{int}$  is:

$$H = \hbar \begin{pmatrix} 0 & \frac{\Omega_p}{2} e^{i\omega_p t} & 0 \\ \frac{\Omega_p}{2} e^{-i\omega_p t} & \omega_1 & \frac{\Omega_c}{2} e^{i\omega_c t} \\ 0 & \frac{\Omega_c}{2} e^{-i\omega_c t} & \omega_1 + \omega_2 \end{pmatrix}. \quad (1.9)$$

We can get rid of the temporal dependency by means of a transformation to the rotating frame:

$$\tilde{H} = U H U^\dagger + i\hbar (\partial_t U) U^\dagger \quad (1.10)$$

using the unitary matrix:

$$U = \exp(i\omega_p t |e\rangle\langle e| + i(\omega_p + \omega_c) t |r\rangle\langle r|), \quad (1.11)$$

the resulting Hamiltonian after the transformation is:

$$\tilde{H} = \hbar \begin{pmatrix} 0 & \frac{\Omega_p}{2} & 0 \\ \frac{\Omega_p}{2} & -\delta_1 & \frac{\Omega_c}{2} \\ 0 & \frac{\Omega_c}{2} & -\delta_1 - \delta_2 \end{pmatrix}. \quad (1.12)$$

### 1.1.2 Master Equation

Let us include some non-unitary processes, like decays, through the density matrix treatment. The master equation we want to study here is [14]:

$$\partial_t \tilde{\rho} = -\frac{i}{\hbar} [\tilde{H}, \tilde{\rho}] + \Gamma_1 \mathcal{D}[\sigma_1] \tilde{\rho} + \Gamma_2 \mathcal{D}[\sigma_2] \tilde{\rho} + \gamma_g \mathcal{D}[\sigma_g] \tilde{\rho}, \quad (1.13)$$

where  $\tilde{\rho}$  is the density matrix in the rotating frame,  $\Gamma_1$  is the decay rate from state  $|e\rangle$  to  $|g\rangle$ ,  $\Gamma_2$  is the decay rate from  $|r\rangle$  to  $|e\rangle$ ,  $\gamma_g$  contains all the processes of loss of coherence between states,  $\sigma_g = |g\rangle\langle g| - |r\rangle\langle r|$ , and the Lindblad superoperator is defined as [14]:

$$\mathcal{D}[c] \tilde{\rho} = c\tilde{\rho}c^\dagger - \frac{1}{2} (c^\dagger c\tilde{\rho} + \tilde{\rho}c^\dagger c). \quad (1.14)$$

### 1.1.3 Electric susceptibility

Through equation 1.13 we can predict the optical response of the three level atom when it is stimulated with two electric fields. The polarization of the medium is given by:

$$\mathbf{P}^{(+)} = \epsilon_0 \chi \mathbf{E}^{(+)}, \quad (1.15)$$

where  $\epsilon_0$  is the electric permittivity of the vacuum and  $\chi$  is the linear susceptibility, the latter is linked to the refractive index and the absorption properties. We can analyze the response of the three level atom only to the probe beam, in this case we can relate the polarization of a whole atomic ensemble with the dipole moment as:

$$\mathbf{P}^{(+)} = N \langle \mathbf{d}^{(+)} \rangle = N \langle g | \mathbf{d} | e \rangle \tilde{\rho}_{eg}, \quad (1.16)$$

with  $N$  the numerical density of the atoms. In equations 1.15 and 1.16 we have terms oscillating at two different frequencies for the probe and control beam, but our detector can only measure the former. The susceptibility for the probe field is therefore:

$$\chi = \frac{2N \langle g | \hat{\epsilon}_p \cdot \mathbf{d} | e \rangle}{\epsilon_0 E_p} \tilde{\rho}_{eg} = -\frac{2N \langle g | \hat{\epsilon}_p \cdot \mathbf{d} | e \rangle^2}{\epsilon_0 \Omega_p \hbar} \tilde{\rho}_{eg}. \quad (1.17)$$

Through the master equation 1.13 we calculate the matrix element  $\tilde{\rho}_{eg}$  as:

$$\begin{aligned} \partial_t \tilde{\rho}_{eg} &= \left[ -\frac{\Gamma_1}{2} + i\delta_1 - \frac{\gamma_g}{2} \right] \tilde{\rho}_{eg} + \frac{i\Omega_p}{2} (\rho_{ee} - \rho_{gg}) - \frac{i\Omega_c}{2} \tilde{\rho}_{rg} \\ &\approx \left[ -\frac{\Gamma_1}{2} + i\delta_1 - \frac{\gamma_g}{2} \right] \tilde{\rho}_{eg} - \frac{i\Omega_p}{2} - \frac{i\Omega_c}{2} \tilde{\rho}_{rg}, \end{aligned} \quad (1.18)$$

where the approximations  $\rho_{gg} \approx 1$  and  $\rho_{ee} \approx 0$  have been made, this is equivalent to having a weak probe beam. The equation 1.18 is coupled to the matrix element  $\tilde{\rho}_{rg}$  and we calculate it in the same way:

$$\begin{aligned} \partial_t \tilde{\rho}_{rg} &= \left[ -\frac{\Gamma_2}{2} + (\delta_1 + \delta_2) - 2\gamma_g \right] \tilde{\rho}_{rg} - \frac{i\Omega_c}{2} \tilde{\rho}_{eg} - i\frac{\Omega_p}{2} \tilde{\rho}_{re} \\ &\approx \left[ -\frac{\Gamma_2}{2} + (\delta_1 + \delta_2) - 2\gamma_g \right] \tilde{\rho}_{rg} - \frac{i\Omega_c}{2} \tilde{\rho}_{eg}, \end{aligned} \quad (1.19)$$

in this we took  $\Omega_p$  small, again the weak probe beam approximation. On the other hand when we solve for the matrix element  $\tilde{\rho}_{re}$  we find that it has a small value, then we can get rid of the term with  $\Omega_p \tilde{\rho}_{re}$ .

Solving equation 1.19 for  $\tilde{\rho}_{rg}$  in the stationary case ( $\partial_t \tilde{\rho}_{rg} = 0$ ) we find:

$$\tilde{\rho}_{rg} = \frac{\Omega_c \tilde{\rho}_{eg}}{2 [i\Gamma_2/2 + (\delta_1 + \delta_2) + 2i\gamma_g]}, \quad (1.20)$$

substituting this into equation 1.18 we get:

$$\tilde{\rho}_{eg} = \frac{(i\Omega_p/2) [-\Gamma_2/2 + i(\delta_1 + \delta_2) - 2\gamma_g]}{[-\Gamma_2/2 + i(\delta_1 + \delta_2) - 2\gamma_g] [-\Gamma_1/2 + i\delta_1 - \gamma_g/2] - (i\Omega_c/2)^2}. \quad (1.21)$$

Finally the value of the linear susceptibility is:

$$\chi = -i \frac{N \langle g | \hat{\epsilon}_p \cdot \mathbf{d} | e \rangle^2}{\hbar \epsilon_0} \frac{[-\Gamma_2/2 + i(\delta_1 + \delta_2) - 2\gamma_g]}{[-\Gamma_2/2 + i(\delta_1 + \delta_2) - 2\gamma_g] [-\Gamma_1/2 + i\delta_1 - \gamma_g/2] - (i\Omega_c/2)^2}. \quad (1.22)$$

In the next section we will explore a very important phenomenon derived from this expression.

## 1.2 Electromagnetically induced transparency

The interaction of the three level atom with the control laser on resonance ( $\delta_2 = 0$ ) lead to quantum interference in the amplitudes of optical transitions. This interference between the excitation pathways change the optical response and eliminates the absorption at the resonant frequency of the transition from ground state to the first excited state. This phenomenon is termed electromagnetically induced transparency (EIT) [9].

The importance of EIT is that it gives rise to greatly enhanced nonlinear susceptibility in the transparency region and this is associated with steep dispersion of the light [15, 16]. The linear response of our three level atom to resonant light is given by the electric susceptibility of equation 1.22. The imaginary part  $\text{Im}[\chi]$  determines the dissipation of the field or absorption and the real part  $\text{Re}[\chi]$  creates a dispersive phase shift. Both functions are shown in figure 1.2. We can see a large gradient of the refractive index close to the atomic resonance as well as a

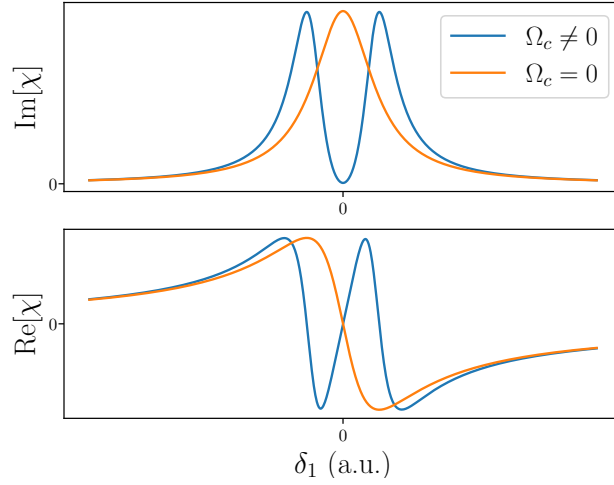


Figure 1.2: Imaginary and real parts of the three level atom electric susceptibility as function of  $\delta_1$ .

negligible absorption. This has dramatic consequences as the speed of propagation of a pulse with frequency  $\omega$  is determined by the group velocity as:

$$v_g = \frac{c}{n_r(\omega) + \omega \frac{dn_r}{d\omega}}, \quad (1.23)$$

therefore, optical pulses propagate in this kind of atomic gases with group velocities tens of millions times slower than pulses traveling in vacuum [17].

### 1.2.1 Dressed-state picture and dark state

We can look at the energies and eigenvalues of the Hamiltonian 1.12 in terms of the mixing angles  $\theta$  and  $\phi$  that are dependent in a simple way upon Rabi frequencies as well as the single photon detuning  $\delta_1$ . In the scenario where  $\delta_1 = -\delta_2$  we have:

$$\tan \theta = \frac{\Omega_p}{\Omega_c} \quad (1.24)$$

and

$$\tan 2\phi = \frac{\sqrt{\Omega_p^2 + \Omega_c^2}}{\delta_1}. \quad (1.25)$$



This eigenstates are written in terms of the bare atom states are:

$$\begin{aligned} |a^+\rangle &= \sin\theta \sin\phi |g\rangle + \cos\phi |e\rangle + \cos\theta \sin\phi |r\rangle \\ |a^0\rangle &= \cos\theta |g\rangle - \sin\theta |r\rangle \\ |a^-\rangle &= \sin\theta \cos\phi |g\rangle - \sin\phi |e\rangle + \cos\theta \cos\phi |r\rangle. \end{aligned} \quad (1.26)$$

These are known as the dressed states. While the state  $|a^0\rangle$  remains at zero energy, the other two states are shifted up and down by the energies:

$$\Delta E_{\pm} = \frac{\hbar}{2} \left( \delta \pm \sqrt{\delta^2 + \Omega_p^2 + \Omega_c^2} \right). \quad (1.27)$$

Moreover, the states  $|a^+\rangle$  and  $|a^-\rangle$  retain a component of all the bare atomic states, but  $|a^0\rangle$  has no contribution from the first excited state therefore this is the dark state since there won't be any spontaneous emission from  $|e\rangle$ .

We can understand EIT from this dressed-state picture. Consider the case of weak probe beam  $\Omega_p \ll \Omega_c$ , thus  $\sin\theta \rightarrow 0$  and  $\cos\theta \rightarrow 1$ , the ground state becomes identical to the dark state and excitation is impossible giving place to EIT. Additionally if  $\delta_1 = 0$  probe beam is on resonance and  $\tan\phi \rightarrow 1$  and then  $|a^+\rangle = (1/\sqrt{2})(|e\rangle + |r\rangle)$  and  $|a^-\rangle = (1/\sqrt{2})(|e\rangle - |r\rangle)$ , these are the relevant states to EIT in the limit of strong coupling beam and weak probe field.

### 1.2.2 Optical response

We want to know what would be the response of the probe beam through a cold atomic cloud under EIT conditions. Suppose the electric field of the probe beam traveling in the  $z$  direction is:

$$E_p(z, t) = \text{Re} \left\{ E_0 e^{i(k_0 n z - \omega t)} \right\}, \quad (1.28)$$

where  $n$  is the refractive index in the media, we can break down this into his real and complex parts  $n = n_r + n_i$  and we have:

$$E_p(z, t) = \text{Re} \left\{ E_0 e^{-k_0 n_i z} e^{i(k_0 n_r - \omega t)} \right\}, \quad (1.29)$$

and the intensity of this field is given by:

$$\begin{aligned} I_p(z) &= E_p E_p^* \\ &= I_0 e^{-2k_0 n_i z}. \end{aligned} \quad (1.30)$$

Now let us recall the Beer-Lambert law which states a relation between the input intensity

of the light passing through a medium and the output intensity:

$$I_{out} = I_{in} e^{-\int_0^{L_z} \alpha(x,y,z) dz}, \quad (1.31)$$

where  $\alpha(x, y, z)$  is the absorption coefficient of de medium which is dependent on the position. If we compare equation 1.30 and the right side of equation 1.31 we can see that:

$$\alpha(x, y, z) = 2k_0 n_i(x, y, z), \quad (1.32)$$

with the wave vector  $k_0 = 4\pi/\lambda$ . Now we can relate the refractive index with our three level atom via the electric susceptibility as follows:

$$n = \sqrt{\epsilon_r \mu_r}, \quad (1.33)$$

where  $\epsilon_r$  is the relative permittivity and  $\mu_r$  is the relative permeability of the three level atom, for an atomic gas  $\mu_r \approx 1$ , thus:

$$\begin{aligned} n &\approx \sqrt{\epsilon_r} = \sqrt{1 + \chi} \\ &\approx 1 + \frac{\chi}{2}, \end{aligned} \quad (1.34)$$

for small values of  $\chi$ . We had already calculated the electric susceptibility for this system in equation 1.22, thus the absorption coefficient for the three level atom is:

$$\begin{aligned} \int_0^{L_z} \alpha(x, y, z) dz &= \frac{4\pi}{\lambda} \int_0^{L_z} n_i(x, y, z) dz \\ &= \frac{2\pi}{\lambda} \int_0^{L_z} \text{Im} \{ \chi(x, y, z) \} dz, \end{aligned} \quad (1.35)$$

finally we get:

$$\alpha(x, y) = \frac{2\pi}{\lambda} \text{Im} \left\{ -i \frac{N(x, y) \langle g | \hat{\epsilon}_p \cdot \mathbf{d} | e \rangle^2}{\hbar \epsilon_0} \frac{[-\Gamma_2/2 + i(\delta_1 + \delta_2) - 2\gamma_g]}{[-\Gamma_2/2 + i(\delta_1 + \delta_2) - 2\gamma_g] [-\Gamma_1/2 + i\delta_1 - \gamma_g/2] - (i\Omega_c/2)^2} \right\}, \quad (1.36)$$

where the integral was calculated over the numerical density of the atoms  $\int_0^{L_z} N(x, y, z) dz = N(x, y)$ . Under EIT conditions  $\delta_2 = 0$  and we can scan  $\delta_1$  around 0 as depicted in figure 1.3.

Whenever we are fitting a function to experimental data of EIT we must convolve the absorption profile with the linewidth of a laser subjected to a feedback system which in most cases it will be a Gaussian function [18]. We can see in figure 1.4 that wider Gaussian profile distorts the original EIT profile. The information of both profiles is present in the convolution.

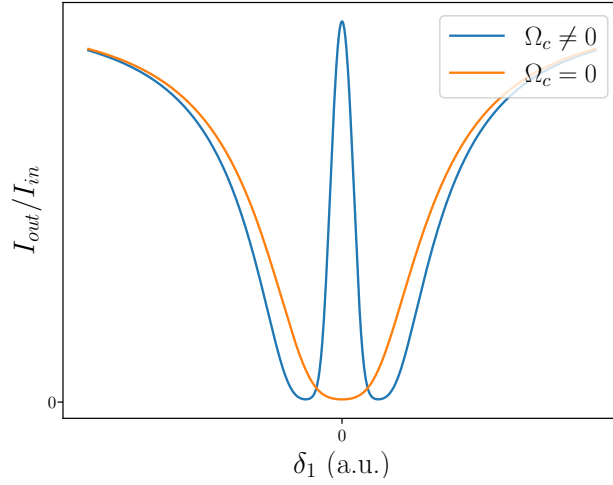


Figure 1.3: Absorption profile of the three level atom under electromagnetically induced transparency ( $\delta_2 = 0$ ) with the control beam on (blue) and off (orange).

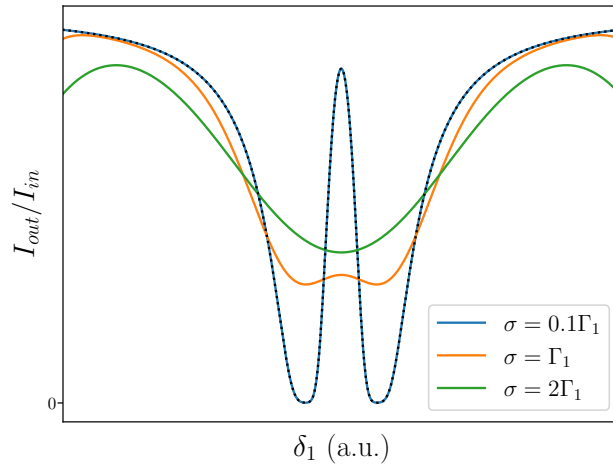


Figure 1.4: Convolution between the absorption profile of the three level atom under EIT and different Gaussian profiles. The full width half maximum of the Gaussian functions is  $2.35\sigma$ . The dotted line is the original EIT profile.

### 1.2.3 Hyperfine structure

In the laboratory we deal with real atoms and their hyperfine structure will be relevant. The treatment is much the same as presented in subsections 1.1.1 and 1.1.2 but some considerations must be made. This subsection is based on [14].

We will consider transitions from a manifold of ground hyperfine levels  $\{|g, m_F\rangle\}$  to a

manifold of first excited hyperfine levels  $\{|e, m_F\rangle\}$ . From the first excited hyperfine manifold we consider transitions to a manifold of Rydberg fine levels  $\{|r, m_J\rangle\}$  as hyperfine structure is not relevant for this highly excited states.

Here we express the Hamiltonian as:

$$H = H_A + H_{int} + H_Z, \quad (1.37)$$

where  $H_A$  is the atomic Hamiltonian,  $H_{int}$  is the atom-field interaction Hamiltonian and  $H_Z$  is the magnetic interaction Hamiltonian. We can express the atomic Hamiltonian in the RWA and in the rotating frame as before like:

$$H_A = \hbar \sum_{m_F} |e, m_F\rangle \langle e, m_F| (-\delta_1) + \hbar \sum_{m_J} |r, m_J\rangle \langle r, m_J| (-\delta_1 - \delta_2). \quad (1.38)$$

Considering a magnetic field along the quantization axis the magnetic interaction Hamiltonian takes the form:

$$H_Z = \sum_{m_F} g_g \mu_B B m_F |g, m_F\rangle \langle g, m_F| + \sum_{m_F} g_e \mu_B B m_F |e, m_F\rangle \langle e, m_F| + \sum_{m_J} g_r \mu_B B m_J |r, m_J\rangle \langle r, m_J|, \quad (1.39)$$

where  $g_g$ ,  $g_e$  and  $g_r$  are the Landé g-factors,  $B$  is the magnetic field and  $\mu_B$  is the Bohr's magneton. For the atomic Hamiltonian we have:

$$H_{int} = -\mathbf{d} \cdot (\mathbf{E}_p + \mathbf{E}_c) = -\sum_q d_q (E_{p,q} + E_{c,q}), \quad (1.40)$$

where  $q$  is an index for the components of the electric fields that are the same as defined in the last section. Again we decompose the dipole operator with the unity matrix that takes the form:

$$\mathbb{1} = \sum_{m_F} |g, m_F\rangle \langle g, m_F| + \sum_{m_F} |e, m_F\rangle \langle e, m_F| + \sum_{m_J} |r, m_J\rangle \langle r, m_J|. \quad (1.41)$$

In this way the dipole operator looks like:

$$\begin{aligned} \mathbf{d} = & \sum_{m_F} \sum_{m'_F} |g, m_F\rangle \langle g, m_F| \mathbf{d} |e, m'_F\rangle \langle e, m'_F| + \sum_{m_F} \sum_{m'_J} |e, m_F\rangle \langle e, m_F| \mathbf{d} |r, m'_J\rangle \langle r, m'_J| + \\ & + \sum_{m_F} \sum_{m'_F} |e, m_F\rangle \langle e, m_F| \mathbf{d} |g, m'_F\rangle \langle g, m'_F| + \sum_{m_J} \sum_{m'_F} |r, m_J\rangle \langle r, m_J| \mathbf{d} |e, m'_F\rangle \langle e, m'_F|. \end{aligned} \quad (1.42)$$

We can use the Wigner-Eckart theorem to simplify the last expression as the expected values of the dipolar operator can be separated as a Clebsch-Gordan coefficient and a reduced matrix

element independent of angular momentum as we describe in more detail in the next chapter in equations 2.4 and 2.8. Therefore we can express equation 1.42 as:

$$\mathbf{d} = \langle J || \mathbf{d} || J' \rangle \left[ \sum_q^{ge} + \sum_q^{ge\dagger} + \sum_q^{er} + \sum_q^{er\dagger} \right], \quad (1.43)$$

where the new introduced terms are the atomic operators for this system:

$$\begin{aligned} \sum_q^{ge} &= \sum_{m_F} \sum_{m'_F} (-1)^{F'+J+1+I} \sqrt{(2F'+1)(2J+1)} \begin{Bmatrix} J & J' & 1 \\ F' & F & 1 \end{Bmatrix} |g, m_F\rangle \langle e, m'_F| \\ \text{and} & \\ \sum_q^{er} &= \sum_{m_F} \sum_{m'_J} \sqrt{(2F+1)(2J+1)} (-1)^{J+J'-I-1+m_F+m'_J+q} \times \\ &\quad \begin{pmatrix} J & I & F \\ m'_J+q & m_F-m'_J-q & -m_F \end{pmatrix} \begin{pmatrix} J' & 1 & J \\ m'_J & q & -m'_J-q \end{pmatrix} |e, m_F\rangle \langle r, m'_J|. \end{aligned} \quad (1.44)$$

The constant terms for this operators are described in section 2.2.

Now lets plug in the equation 1.43 in the interaction Hamiltonian equation 1.40 adding the explicit expression for the electric fields:

$$\begin{aligned} H_{int} &= -\langle J || \mathbf{d} || J' \rangle \sum_q \left( \sum_q^{ge} + \sum_q^{ge\dagger} + \sum_q^{er} + \sum_q^{er\dagger} \right) \times \\ &\quad \left( \frac{E_p \varepsilon_q^p}{2} [e^{i\omega_p t} + e^{-i\omega_p t}] + \frac{E_c \varepsilon_q^c}{2} [e^{i\omega_c t} + e^{-i\omega_c t}] \right). \end{aligned} \quad (1.45)$$

Lets examine the terms we will get from this multiplication, there are terms that only relate to probe beams and others to control beams for this we only will keep the terms containing one positive and one negative frequency term as they oscillate at rates we can observe in the laboratory. On the other hand, there are cross terms between probe and control beams that cannot be detected as they oscillate at very high frequencies because  $\omega_p$  and  $\omega_c$  are very different. In this way we implement a rotating wave approximation and the interaction Hamiltonian looks like:

$$H_{int} = \frac{\hbar}{2} \sum_q \left( \left[ \sum_q^{ge} e^{i\omega_p t} + \sum_q^{ge\dagger} e^{-i\omega_p t} \right] \Omega_q^p + \left[ \sum_q^{er} e^{i\omega_c t} + \sum_q^{er\dagger} e^{-i\omega_c t} \right] \Omega_q^c \right) \quad (1.46)$$

where

$$\Omega_q^p = -\frac{\langle J || \mathbf{d} \cdot \varepsilon_q^p || J' \rangle E_p}{\hbar} \quad \text{and} \quad \Omega_q^c = -\frac{\langle J || \mathbf{d} \cdot \varepsilon_q^c || J' \rangle E_c}{\hbar} \quad (1.47)$$

are the Rabi frequencies of the system. Finally we write the interaction Hamiltonian in the

rotating frame:

$$\tilde{H}_{int} = \frac{\hbar}{2} \sum_q \left( \left[ \sum_q^{ge} + \sum_q^{ge\dagger} \right] \Omega_q^p + \left[ \sum_q^{er} + \sum_q^{er\dagger} \right] \Omega_q^c \right). \quad (1.48)$$

Once we have described the complete Hamiltonian we establish the master equation to introduce non unitary processes:

$$\partial_t \tilde{\rho} = -\frac{i}{\hbar} [\tilde{H}, \tilde{\rho}] + \Gamma_1 \mathcal{D} \left[ \sum_q^{ge} \right] \tilde{\rho} + \Gamma_2 \mathcal{D} \left[ \sum_q^{er} \right] \tilde{\rho}, \quad (1.49)$$

where  $\tilde{\rho}$  is the density matrix in the rotating frame,  $\Gamma_1$  is the decay rate from states on manifold  $\{|e, m_F\rangle\}$  to states in  $\{|g, m_F\rangle\}$ ,  $\Gamma_2$  is similar but from  $\{|r, m_J\rangle\}$  to  $\{|e, m_F\rangle\}$ . Through this equation we will find the susceptibility as follows. We can write the polarization for the positive frequencies of the atomic assembly as:

$$P_q^{(+)} = N \langle d_q \rangle^{(+)} = N = \text{Tr}[\tilde{\rho} d_q]^{(+)}, \quad (1.50)$$

again,  $N$  is the numerical density of atoms. As we are only focusing on the positive frequencies of the system we can write:

$$P_q^{(+)} = N \langle J || \mathbf{d} || J' \rangle \text{Tr} \left[ \left( \sum_q^{ge\dagger} + \sum_q^{er\dagger} \right) \tilde{\rho} \right]. \quad (1.51)$$

On the other hand we can express the polarizability as:

$$P_q^{(+)} = \epsilon_0 \sum_k \chi_{qk} (E_k^p + E_k^c). \quad (1.52)$$

To find every component of  $\chi_{qk}$  one must select one polarization component  $k$  and solve the equation system. Suppose we choose  $k = 0$  for  $\pi$  polarization, therefore:

$$\epsilon_0 \chi_{q0} (E_0^p + E_0^c) = N \langle J || \mathbf{d} || J' \rangle \left( \text{Tr} \left[ \sum_q^{ge\dagger} \tilde{\rho} \right] + \text{Tr} \left[ \sum_q^{er\dagger} \tilde{\rho} \right] \right). \quad (1.53)$$

On both sides of equation 1.53 there are terms that oscillate with the frequency of the probe and control beams but our detectors can measure only one so we chose the probe beam and solve for the susceptibility:

$$\chi_{q0} = \frac{N \langle J || \mathbf{d} \cdot \boldsymbol{\varepsilon}_0^p || J' \rangle}{\epsilon_0 E_0^p} \text{Tr} \left[ \sum_q^{ge\dagger} \tilde{\rho} \right] = -\frac{N \langle J || \mathbf{d} \cdot \boldsymbol{\varepsilon}_0^p || J' \rangle^2}{\epsilon_0 \Omega_0^p \hbar} \text{Tr} \left[ \sum_q^{ge\dagger} \tilde{\rho} \right]. \quad (1.54)$$

From here we just need to follow the same procedure described in subsection 1.2.2 to find the optical response of this atomic medium.

## Chapter 2

---

---

# Rubidium

---

---

2.1	Electronic configuration . . . . .	17
2.1.1	D2 transition . . . . .	19
2.2	Rydberg states . . . . .	21
2.2.1	Rydberg transitions . . . . .	22
2.2.2	Energy levels . . . . .	23

In this chapter we describe the atomic system we selected for our experiment. Rubidium, as well as lithium, sodium, potassium, cesium and francium, has only one valence electron and this group of atoms is known as alkali atoms. This simple electronic configuration gives us experimental advantages for the manipulation of its quantum states and generation of Rydberg atoms.

For rubidium there are a lot of benefits, the laser wavelengths for the generation of the first excited state and Rydberg excitation are easily generated with commercial lasers, the literature and study of rubidium atomic physics is vast and there are a wide range of experiments based on this alkali atom.

In the first section of this chapter we present the electronic configuration of rubidium's ground state and the transition to the first excited state. Then we introduce all the relevant physics to the study and generation of Rydberg atoms effectively creating a three level atom.

### 2.1 Electronic configuration

Rubidium is a very soft grey alkali metal. Natural rubidium comprises two isotopes:  $^{85}\text{Rb}$  and  $^{87}\text{Rb}$ . Some of their relevant characteristics are listed on table 2.1.

Isotope	Abundance	Half-life (years)	Mass (u)	Nuclear spin
$^{85}\text{Rb}$	72.168%	Stable	84.911789739(9)	$I = 5/2$
$^{87}\text{Rb}$	27.835%	$4.88 \times 10^{10}$	86.909180535(10)	$I = 3/2$

Table 2.1: Relevant characteristics of isotopes  $^{85}\text{Rb}$  and  $^{87}\text{Rb}$ .

The atomic number of rubidium is 37, its ground state has the following electronic configuration:

$$1s^2 2s^2 2p^6 3s^2 3p^6 3d^{10} 4s^2 4p^6 5s, \quad (2.1)$$

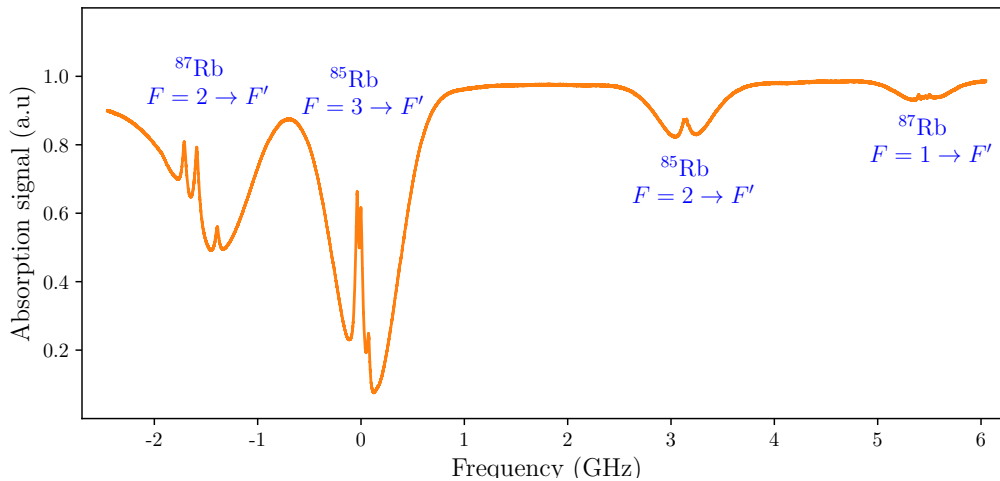
this means the first excited state of rubidium is the 5p state. As we introduce the spin-orbit interaction fine structure of the atoms becomes important and we label the ground state as  $5^2S_{1/2}$  while the first excited state unfolds into  $5^2P_{1/2}$  and  $5^2P_{3/2}$ .

Finally, as we count all the effects due to angular momentum of the nucleus we have de hyperfine structure. The ground state for  $^{85}\text{Rb}$  has  $F = 2, 3$  where  $F$  accounts for the total angular momentum, and for  $^{87}\text{Rb}$   $F = 1, 2$ . In this scheme, and following the selection rules for electric dipole transition, we have two lines of transition from ground state of rubidium to the first excited state named D1 and D2 lines:

$$\text{D1: } 5^2S_{1/2} \rightarrow 5^2P_{1/2}$$

$$\text{D2: } 5^2S_{1/2} \rightarrow 5^2P_{3/2}.$$

In the figure 2.1 we show the saturated absorption spectroscopy [19] of the D2 line for  $^{85}\text{Rb}$  and  $^{87}\text{Rb}$ .

Figure 2.1: Measured saturated absorption spectroscopy of line D2 of  $^{85}\text{Rb}$  and  $^{87}\text{Rb}$ .



### 2.1.1 D2 transition

Now that we have the electronic structure of rubidium we want to study the D2 transition to generate EIT and cool the atoms. As the hyperfine structure becomes relevant our objective is to understand the hyperfine transitions of the  $5^2S_{1/2} \rightarrow 5^2P_{3/2}$  excitation path and their relative probabilities.

To find the relative probabilities we need to calculate the dipolar operator matrix elements between the different possible transitions. In this case the dipole operator for a microelectronic atom is:

$$\mathbf{d} = \sum_{i=1}^N -e\mathbf{r}_i. \quad (2.2)$$

For alkali atoms the parity of the dipolar operator is defined by the valence electron. To find the matrix elements we can use the Wigner-Eckart theorem, which allows us to pull apart the matrix elements into one part which is independent of angular momentum projection and the other which is a Clebsch-Gordan coefficient [20]. In this case we have [14]:

$$\begin{aligned} \langle Fm_F | d_q | F'm'_F \rangle &= \langle F || D || F' \rangle \langle Fm_F | F'm'_F; 1q \rangle \\ &= \langle F || D || F' \rangle (-1)^{F'-F+m'_F-m_F} \sqrt{\frac{2F+1}{2F'+1}} \langle F'm_F | Fm_F; 1-q \rangle, \end{aligned} \quad (2.3)$$

where  $q$  takes the values: 1 for  $\sigma_+$  polarized light that increases  $m_F$  by one, -1 for  $\sigma_-$  polarized light that decreases  $m_F$  by one and 0 for  $\pi$  polarized light that leaves  $m_F$  with the same value. We can go further in equation 2.3 replacing the value of  $\langle F || D || F' \rangle$  :

$$\begin{aligned} \langle F || D || F' \rangle &= \langle JIF || D || J'I'F' \rangle \\ &= \langle J || D || J' \rangle (-1)^{F'+J+1+I} \sqrt{(2F'+1)(2J+1)} \begin{Bmatrix} J & J' & 1 \\ F' & F & 1 \end{Bmatrix}, \end{aligned} \quad (2.4)$$

where the term in braces is the Wigner's 6-j symbol. Finally we can replace  $\langle J || D || J' \rangle$  :

$$\begin{aligned} \langle J || D || J' \rangle &= \langle LSJ || D || L'S'J' \rangle \\ &= \langle L || D || L' \rangle (-1)^{J'+L+1+S} \sqrt{(2J'+1)(2L+1)} \begin{Bmatrix} L & L' & 1 \\ J' & J & S \end{Bmatrix}. \end{aligned} \quad (2.5)$$

Using equations 2.3 and 2.4 we can write the relative transition probabilities between different  $m_F$  of ground state in  $^{85}\text{Rb}$  and  $^{87}\text{Rb}$  and  $m'_F$  in their first excited states. In [21] and [22] we can look for all possible excitation paths with field polarizations and their relative probabilities as multiples of  $\langle J || D || J' \rangle$ .

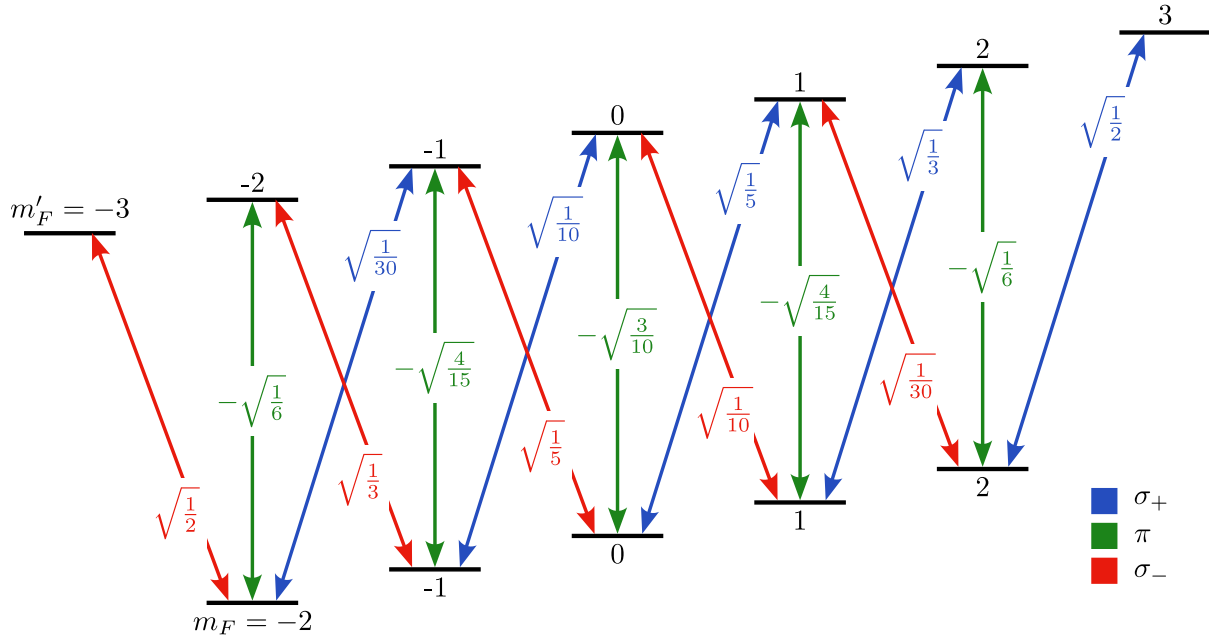


Figure 2.2: The transition matrix elements for  $F = 2 \rightarrow F' = 3$  in  $^{87}\text{Rb}$  expressed as multiples of the reduced dipole matrix elements.

In figures 2.2 and 2.3 are depicted the transitions  $F = 3 \rightarrow F' = 4$  in  $^{85}\text{Rb}$  and  $F = 2 \rightarrow F' = 3$  in  $^{87}\text{Rb}$  and their relative transition probabilities. These are the transitions we will use as the first excitation for the generation of EIT.

An important breakthrough in atomic physics was the development of cooling techniques of atomic gases near the absolute zero of temperature. In this regime the interaction between light and atoms is nearly Doppler free, processes of coherence loss decrease, and in the ultimate limit of Bose-Einstein condensate all the atoms in the cold sample exhibit its quantum mechanical nature in the macroscopic scale. In this work we use the technique of magneto-optical trap [23] to cool a sample of  $^{87}\text{Rb}$  approximately to  $100\ \mu\text{K}$  (see chapter 3).

In the making of a MOT the magnetic projection of the total angular momentum  $m_F$  of the energy levels becomes relevant and the polarization of the light determines the transitions. For alkali atoms two different transitions must be driven to perform laser cooling: a cooling and a repumping transition. The cooling transition serves as the principal mechanism to slow down the velocity of the atoms. It must be a cycling transition, this means that the atom should be given the opportunity to stay cycling between two quantum states without decaying into a dark state and we better chose a highly probable transition. We need to be able to calculate the relative transition probability between all the magnetic projections of ground state and first excited state in rubidium.

As we drive the population of atoms to the cycling transition for cooling some of them will be off-resonantly excited to a level with lower  $F'$ , this will leave the atoms in a dark state for

our cooling beam and they will be lost out of the MOT. To overcome this problem we can drive them again into the cooling transition by coupling a repumping beam. For instance, in  $^{87}\text{Rb}$  we chose for cooling the  $F = 2 \rightarrow F' = 3$  transition but some of the atoms will be excited to  $F' = 2$  as this is more probable [22], from this state it will spontaneous decay to  $F = 1, 2$ . The atoms in  $F = 1$  are in a dark state for the cooling beam and we will need to couple a repumping beam in the transition  $F = 1 \rightarrow F' = 2$  to bring them back into the cooling cycle.

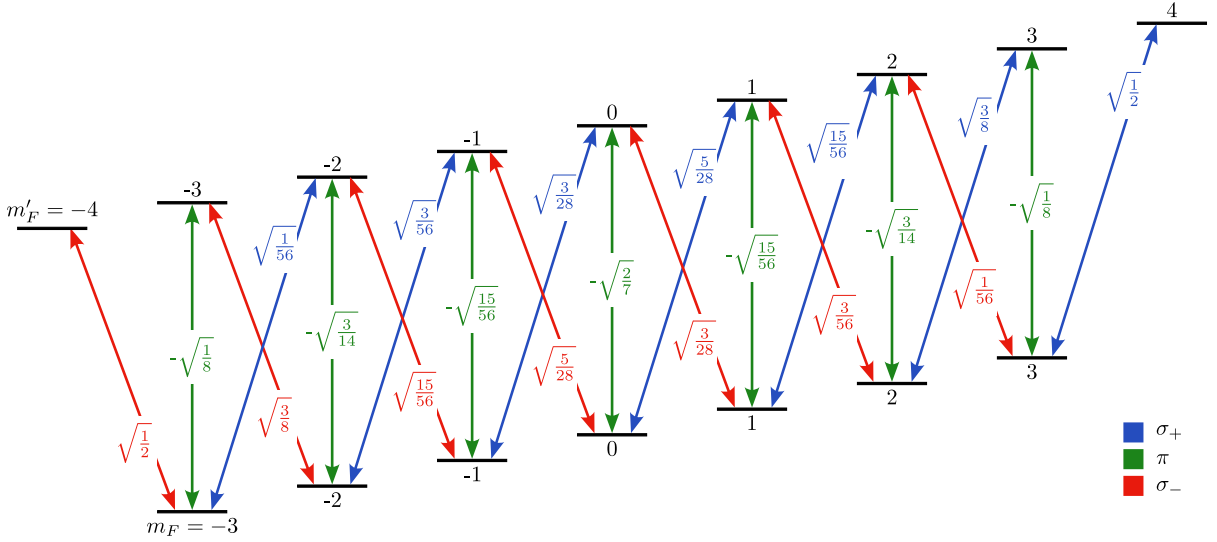


Figure 2.3: The transition matrix elements for  $F = 3 \rightarrow F' = 4$  in  $^{85}\text{Rb}$  expressed as multiples of the reduced dipole matrix elements.

## 2.2 Rydberg states

To effectively create a three level atom in the laboratory we use the control field to excite rubidium atoms from the first excited state  $5^2P_{3/2}$  to a excited state with a high principal quantum number  $n \geq 20$ . This kind of highly excited quantum state are called *Rydberg states* and their properties, like half life or polarizability, scale dramatically with  $n$ .

Atoms in Rydberg states exhibit an interaction with a van der Waals like potential  $U(R) = C_6/R^6$  where  $R$  is the interatomic distance and  $C_6 \propto n^{11}$ . Due to this interaction once a Rydberg atom is generated it creates an energy shift in all surrounding atoms and a second Rydberg excitation is forbidden within a blockade radius, this phenomenon is known as Rydberg blockade. This tool was proposed as a mechanism to obtain cooperative interaction between light and matter and allows us to map dipolar interactions between atoms to a light field [24].

### 2.2.1 Rydberg transitions

In rubidium we have two possible two photon excitations to Rydberg states following the dipole transition selection rules:

$$5S \xrightarrow{780 \text{ nm}} 5P \xrightarrow{480 \text{ nm}} nS/nD, \quad (2.6)$$

an alternative is

$$5S \xrightarrow{420 \text{ nm}} 6P \xrightarrow{1016 \text{ nm}} nS/nD. \quad (2.7)$$

Both schemes are possible with commercial diode lasers and in this work we chose the first one. In this case the dipole transition matrix elements scale as  $\langle 5P | e\mathbf{r}_e | nS \rangle \propto n^{-3/2}$  [25]. Moreover there is a possibility to achieve Rydberg excitations using a single photon transition, but the wavelength of the light is 297 nm and it is hard to produce and manipulate. Also, it does not allow us to study the phenomena of the three level atom. An energy level scheme of rubidium is depicted in figure 2.4.

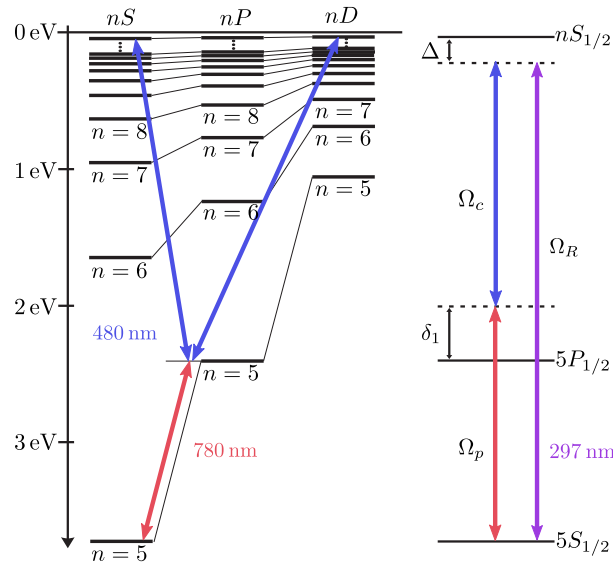


Figure 2.4: Energy levels of the transitions to Rydberg states in rubidium. Rabi frequencies  $\Omega_p$  and  $\Omega_c$  characterizes the interaction strength between probe and control fields and the atoms.  $\Omega_R$  is the Rabi frequency in the single photon transition scheme.

Rydberg levels are specified by the quantum numbers of the single valence electron, these are:  $n$ , the principal quantum number,  $l$ , orbital angular momentum,  $j$ , total angular momentum and  $m_j$ , the magnetic quantum number. The hyperfine structure of Rydberg states is irrelevant for interaction between Rydberg atoms as the typical splitting  $\Delta_{hfs} < 11 \text{ MHz}$  for  $n \gg 40$  cannot be resolved so far. Thus to find the transition matrix elements from first excited state  $5^2P_{3/2}$

to a Rydberg level we need an equation analogue to equation 2.3 [14]:

$$\langle F m_F | d_q | J' m_J' \rangle = \langle J || D || J' \rangle \sqrt{(2F+1)(2J+1)} (-1)^{J+J'-I-1+m_F+m_J'+q} \times \begin{pmatrix} J & I & F \\ m_J+q & m_F-m_J'-q & -m_F \end{pmatrix} \begin{pmatrix} J' & 1 & J \\ m_J' & q & -m_J'-q \end{pmatrix}, \quad (2.8)$$

where the last two terms are Wigner's 3-j symbols. Again,  $q$  is a parameter for the polarization of the light as described in section 2.1. Some of the transition matrix elements for  $5^2P_{3/2} \rightarrow n^2S_{1/2}$  transition in  $^{87}\text{Rb}$  are depicted in figure 2.5 as multiples of  $\langle J || D || J' \rangle$ . One must notice that unlike the transitions described in section 2.1 in this case multiple polarizations will excite the same transition.

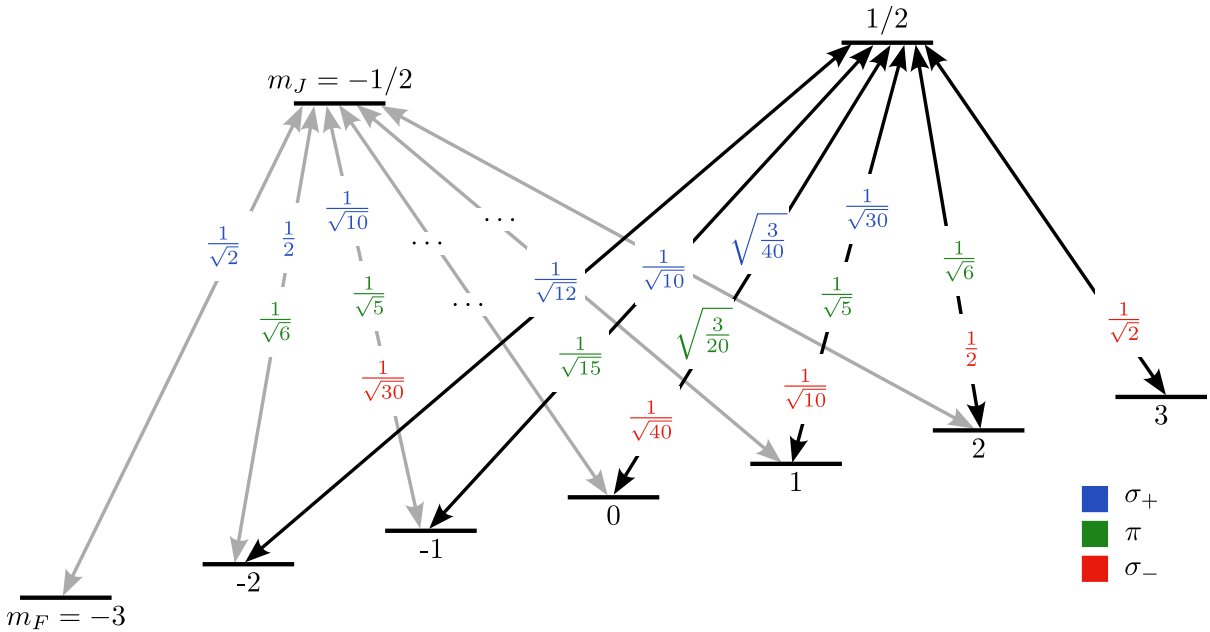


Figure 2.5: The transition matrix elements for  $5^2P_{3/2} \rightarrow n^2S_{1/2}$  in  $^{87}\text{Rb}$  expressed as multiples of the reduced dipole matrix element.

## 2.2.2 Energy levels

Once we have chosen the scheme of excitation to Rydberg levels we should be able to calculate and experimentally produce the correct wavelengths to excite rubidium atoms from state  $5^2P_{3/2}$  to a Rydberg level. A full guide to calculate the dipole matrix elements and interaction potentials in Rydberg states is presented in [26].

The Rydberg energy levels can be calculated in analogy to the Rydberg expression for

hydrogen:

$$E_{nlj} = -\frac{hcR^*}{n^{*2}}, \quad (2.9)$$

where  $n^*$  is a non-integer effective principal quantum number independent for each atomic species and is found to depend strongly on the orbital angular momentum  $l$ . The modified Rydberg constant is:

$$R^* = \frac{1}{1 + m_e/M_{atom}} R_\infty \quad (2.10)$$

and  $M_{atom}$  is the species dependent mass of the atomic core. The energies of the Rydberg series can be expressed through the *quantum defects*, this is,  $n^* = n - \delta_{nlj}$ . This can be written as a series expansion [27]:

$$\delta_{nlj} = \delta_0 + \frac{\delta_2}{(n - \delta_0)^2} + \frac{\delta_4}{(n - \delta_0)^4} + \frac{\delta_6}{(n - \delta_0)^6} + \dots \quad (2.11)$$

The coefficients are obtained from fits to experimentally measured transition energies in each species. The quantum defects decrease rapidly with increasing  $l$ , since for high orbital angular momentum the influence of the core in the valence electron becomes less relevant. The quantum defects have been experimentally determined for Rydberg states with low  $l$ , with the most precise data being for the alkali atoms, a list of references with the coefficients of the quantum defects for the alkali can be found in [26].

Now we want to find the transition wavelengths between state  $5P_{3/2}$  to any Rydberg level  $nS_{1/2}$ , this is relevant as the wavelength is one of the quantities we can measure in the experiment. The way to do this is calculating the energy difference between the quantum states. For the  $5P_{3/2}$  state the energy has been measured to a value of 2.5880 J [28], in this case the quantum defect theory does not give an accurate value due to the proximity of the electron with the nucleus. For the states  $nS_{1/2}$  with  $n > 8$  the quantum defect theory gives us a better result and we can calculate the energy through equation 2.9. Now we can take the energy difference and this will be the transition energy:

$$E_{Rt} = E_p - E_c, \quad (2.12)$$

where  $E_{Rt}$  is the energy for the Rydberg transition,  $E_p$  is the energy of the level  $5P_{3/2}$  and  $E_c$  is the energy of the Rydberg state  $nS_{1/2}$ . From here we just have to find the wavelength of the photon with this energy:

$$\lambda = \frac{hc}{|E_{Rt}|}. \quad (2.13)$$

For the transitions we are interested the wavelength associated to this energy will be around 480 nm.

## Chapter 3

---

---

# Experimental setup

---

---

3.1	Laser system . . . . .	25
3.1.1	Digital locking . . . . .	26
3.1.2	Beatlock rack module . . . . .	30
3.2	Magneto-optical trap . . . . .	31
3.2.1	Vacuum system . . . . .	31
3.2.2	Coils . . . . .	32
3.2.3	Optics . . . . .	33
3.3	EIT with Rydberg states . . . . .	33
3.3.1	Optics . . . . .	33
3.3.2	Sequence and data processing . . . . .	34

In this chapter we describe the most recent advances in the Laboratorio de Óptica Cuántica de Rydberg in UNAM which led us to the creation of a  $^{87}\text{Rb}$  MOT and the observation of Rydberg excitations in this cold atomic cloud. The details of the laser system we used for the generation of Rydberg atoms can be found in [29].

### 3.1 Laser system

In order to generate and measure EIT on a cold atom sample several lasers were needed. The cooling and repumping lasers to cool and contain the atoms in the magneto-optical trap we will discuss in the next section. Also a called probe beam that serves as the first excitation step in the three level atom we studied in chapter 1. In this section we will understand the locking technique we used to tune in the lasers frequency to excite the atomic transitions.

We already discussed the cooling and repumping transitions for  $^{85}\text{Rb}$  and  $^{87}\text{Rb}$  in section 2.1. Since hyperfine splitting of these transitions is large, 2.9 GHz for  $^{85}\text{Rb}$  and 6.9 GHz for  $^{87}\text{Rb}$  (see figure 2.1), we cannot easily derive the laser frequency for repumping from the cooling laser by modulation techniques.

In this work we use three different light sources for cooling, repumping and probe transition. These will be called *secondary* lasers and they are locked to a fourth laser, called the *primary* laser, via a beatnote of their frequencies. The primary laser is locked to a high finesse cavity using the Pound-Drever-Hall method [30]. Locking the beatnote of the lasers allows us to easily change the locking points and scan the transitions to find what is most effective to excite the atoms.

As we said before we use the optical beatnote of the lasers in the locking technique. A beatnote is an oscillation of the optical intensity arising from the superposition of light with different optical frequencies. These oscillations occur at the sum and difference of the lasers frequencies and one can use a photodiode to detect them. Next we describe this locking technique and the construction of our system.

### 3.1.1 Digital locking

The locking system we built is based on the work by Lvovsky et al. [31] and Jasperse [32]. We use an all digital phase detection to phase lock the frequency differences between two lasers ranging from sub-MHz up to 7 GHz.

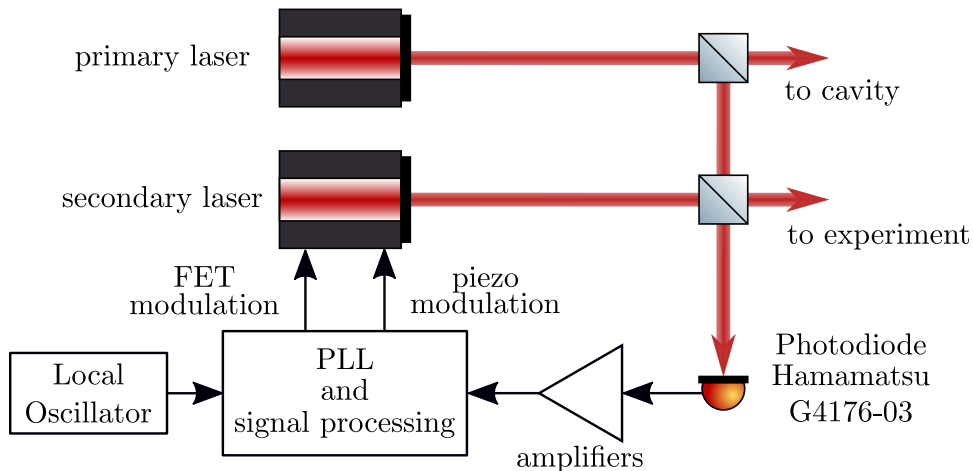


Figure 3.1: Schematic of the digital lock loop. A fraction of the light from primary and secondary lasers are combined on a non polarizing beam splitter (NPBS) to generate a beatnote measured on a photodiode. Signal is amplified and compared to a LO by the PLL to generate the error signal. FET and piezo-electric modulations are fed back to the secondary laser controller to close the loop.



As the beatnote between primary and secondary lasers could be in the microwave regime we use a phase-locked loop (PLL) to divide the beatnote frequency down to the rf-domain where we can easily process it. We use the Analog Devices EVAL-ADF4007EB1 evaluation board of the ADF4007 high frequency divider/ PLL synthesizer. The PLL compares the phase of a local oscillator (LO) and the phase of the frequency divided beatnote to produce an error signal which we use to lock the phase of the beatnote relative to the phase of the LO.

Since the phase of the beatnote depends on the frequency difference of the lasers, that we can adjust through the LO, this effectively locks the frequency of the secondary lasers to the frequency of the primary laser which is locked to a high finesse cavity. The primary laser is locked to the transmission peak of a high finesse cavity. Using a modified PDH technique we can lock the laser to any frequency creating different transmission peaks called sidebands with an electro-optic modulator. For our purposes the sideband frequency matches the  $^{85}\text{Rb}$   $F = 2 \rightarrow F' = 2 \otimes 3$  transition. This sets the zero frequency from where the beatnotes are measured.

In this scheme, see figure 3.1, a fraction of the light from primary and secondary lasers are combined on a non polarizing beam splitter (NPBS) to generate a beatnote measured in a Hamamatsu G4176-03, this is a fast photodiode that has a 30 ps rise time at 7 V bias. We power this photodetector with MiniCircuits ZX85-12G+ Bias-Tee with 9 V DC input and the signal is amplified with MiniCircuits ZX60-8008E+ amplifier up to  $\approx 0$  dBm required to feed the PLL. Since the beatnote for  $^{87}\text{Rb}$  repumping transition is 5.5 GHz a high bandwidth amplifier such as KU LNA BB 0050700 A amplifier from KUHNE was added in this case.

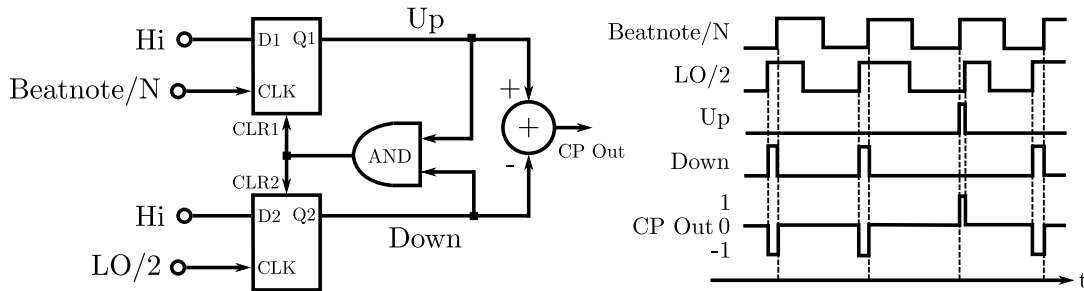


Figure 3.2: Schematic of the PFD functioning. The frequency divided signals of the beatnote and LO are fed into the clock channel of two flip flops. Whenever there is a rise in the clock channels, a high state is written to the Q outputs. They are then compared in the AND gate and whenever they are both equal the system is reset to a low state, otherwise the difference of the signals is delivered in the charge pump (CP) output as the error signal.

The PLL device takes the beatnote signal ( $f_{beat}$ ) and LO signal ( $f_{ref}$ ) with a frequency up to 6 GHz and 240 MHz respectively, and uses counters to frequency divide them by  $N$  and 2 respectively, then it compares them using a phase-frequency detector (PFD) that produces an error signal that quantifies the difference between the measured and desired ( $f_0$ ) beatnote

frequencies. In this case we use a 0 dBm sinusoidal signal generated with a DDS as our LO. A diagram of the general functioning of a PFD is depicted in figure 3.2.

If the compared frequencies are different then the PFD output is set to either 0 V or 5 V depending on which frequency is higher. If the divided frequencies are the same the output is a voltage between 0 V or 5 V that is proportional to their difference in phase. In this way the output signal is a voltage proportional to the difference between the beatnote frequency  $f_{beat}$  and desired frequency  $f_0$ . The error signal is processed and fed to the controller of the secondary lasers to close the loop.

The division factor  $N$  can take the values 8, 16, 32 or 64 and this is selected in combination with  $f_{ref}$  to fix the beatnote frequency as  $f_0 = N f_{ref}/2$ . There is a more versatile version of this system where the value of the counters can be selected in a wider range (Analog EVAL-ADF4108EBZ1) but we find our version is enough to match our purposes.

The range of the signal output by the PLL is 0-5 V, to match the laser controller input specifications we built a signal processing circuit depicted in figure 3.3. The PFD output is fed through a gain-2 offset amplifier that level-shifts the input to be symmetric about zero. Next, a variable gain amplifier includes a protective clamp in the feedback to limit the range of the amplified error signal and prevent the laser entering oscillation.

Since the instantaneous bandwidth of a typical extended cavity diode laser (ECDL) may span a few hundreds of kilohertz the loop must be made as fast as possible in order to correct all the possible noises. To achieve the required frequency range dual feedback was employed. Two branches are derived in this point. We modulate the external cavity length with a piezo-electric transducer to correct for the low frequency noise (slow feedback) and direct modulation of the injection current of the diode for the high frequency components (fast feedback).

There is a special challenge in the feedback for a diode laser. At low modulation frequencies, changes in the diode injection current affects the lasing frequency due to modulation of the recombination area's temperature. At high modulation frequencies what changes is the refractive index of the gain medium. This two mechanisms oppose each other which leads to a phase shift of  $180^\circ$  in modulation frequencies between 1 and 10 MHz. To compensate for this problem we use a phase-advance loop filter followed by a buffer stage with adjustable gain.

To prevent damage to the diode, the control signal was not added directly to the diode, but a FET modulation technique was used, this drains a small amount of current away from the diode in proportion to a control voltage derived from the PFD. The circuit schematics are depicted in figure 3.4. When the beatnote acquires the desired frequency  $f_0$  as the secondary laser scans the PFD output jumps changing the FET base voltage bleeding current from the diode effectively reducing the frequency again. This brings back the laser to the desired frequency linearizing the step function across the scan sweep as depicted in figure 3.5. This allows the slow servo to achieve a lock.

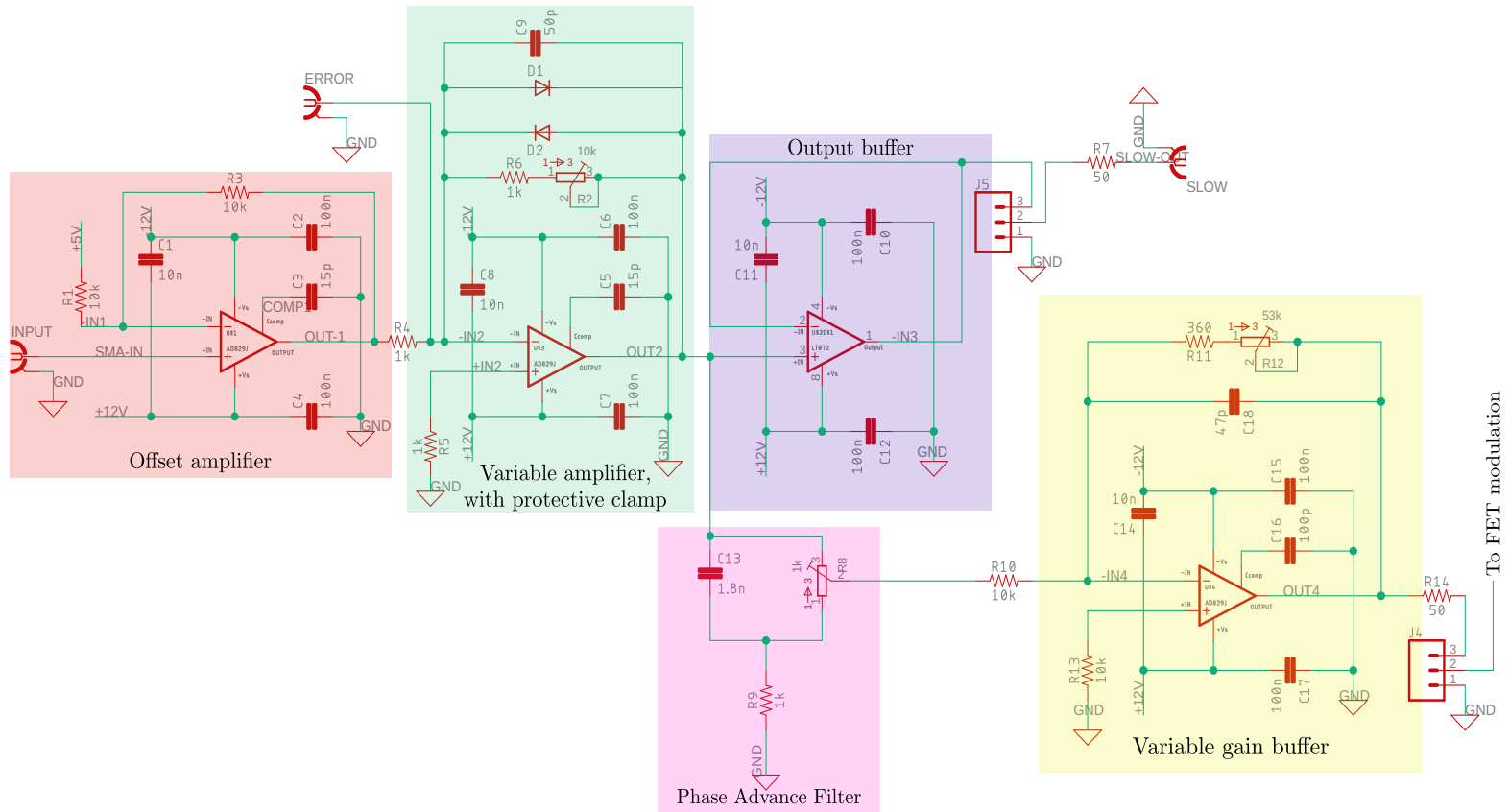


Figure 3.3: Signal processing circuit schematic. The circuit shifts, amplifies, clamps and divide the error signal to produce a slow and fast feedback.

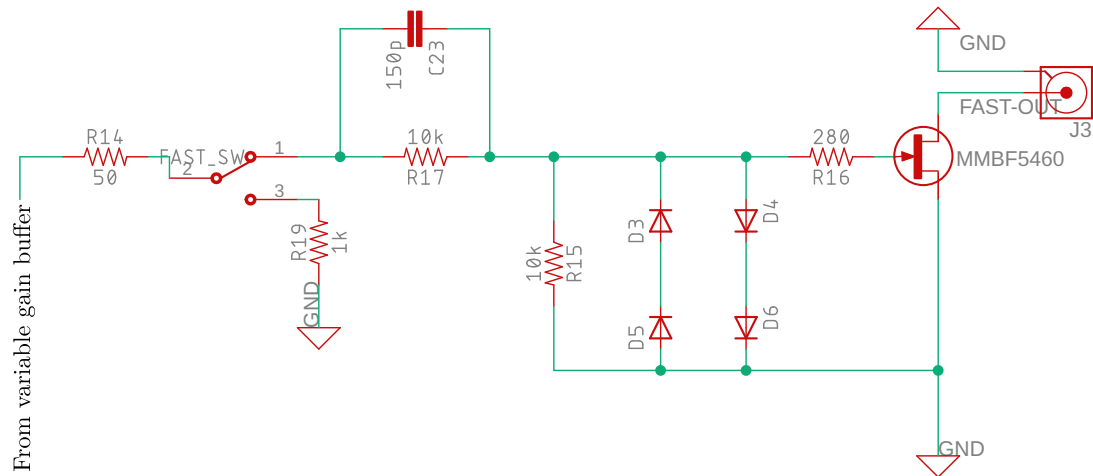


Figure 3.4: FET modulation circuit schematic. A positive voltage causes the JFET to bleed a small amount of current away from the diode.

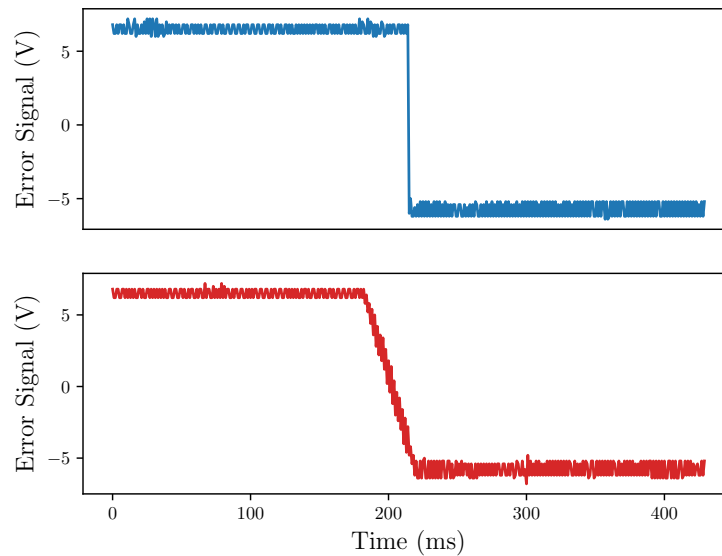


Figure 3.5: Beatnote error signal with FET modulation technique off (blue) and on (red).

### 3.1.2 Beatlock rack module

To implement the digital lock feedback described before we built a rack module shown in figure 3.6. Our beatlock rack module takes the beatnote signal from the photodiode and the LO signal from our home-built DDS rack module based on the Analog Devices AD9959. The beatlock board delivers this signals to the EVAL-ADF4007EB1 and generates the error signal. Then the

signal is processed with the circuit we described before, slow and fast signals are delivered. The slow feedback signal is connected to the laser piezo controller and the fast feedback signal goes directly to the diode current injection. Using this system we successfully locked the cooling, repumping and probe lasers.

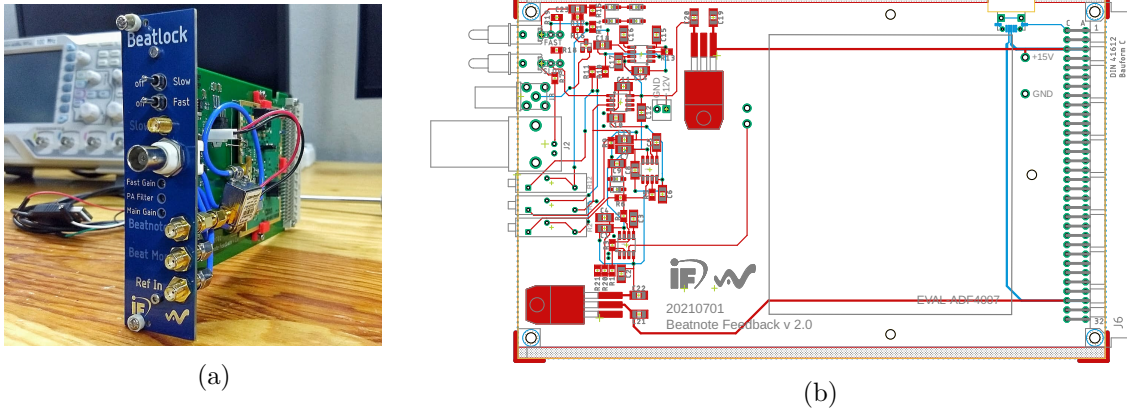


Figure 3.6: Rack module of the beatlock locking system. (a) Rack module assembled. (b) Rack module board layout.

## 3.2 Magneto-optical trap

To cool and trap the atomic sample where we want to perform our experiments we built a magneto-optical trap (MOT). For this we need to implement three pairs of counterpropagating laser beams with the cooling and repumping frequencies we discussed in chapter 2. Two coils form a quadrupole magnetic field which allows a radiative force to be exerted on atoms by the laser beams. These beams intersect at the center of a vacuum chamber that achieves very low pressures that ensures that the cold sample will not be destroyed by background energetic atoms. Now we present a short summary of the most relevant features of our magneto-optical trap. A full guide of this cooling technique can be found in [23].

### 3.2.1 Vacuum system

Our vacuum chamber is designed to perform quantum optics experiments based on Rydberg interactions using a low finesse cavity to enhance interaction between Rydberg atoms and optical fields [33]. In addition to that, a system for ionization of rubidium atoms in Rydberg states and a system of electrodes for compensation of electric fields will be implemented.

In the first stage of our experiment none of the above were installed. We built the vacuum system to use rubidium dispensers and a NEX Torr 200 ionic pump. The system was baked up to 433.15 K for four days and a final pressure of less than  $10^{-10}$  mbar was achieved. This

pressure allows us to generate a cold gas of  $^{87}\text{Rb}$  at  $\approx 100\ \mu\text{K}$ . A photograph of our vacuum system is depicted in figure 3.9.

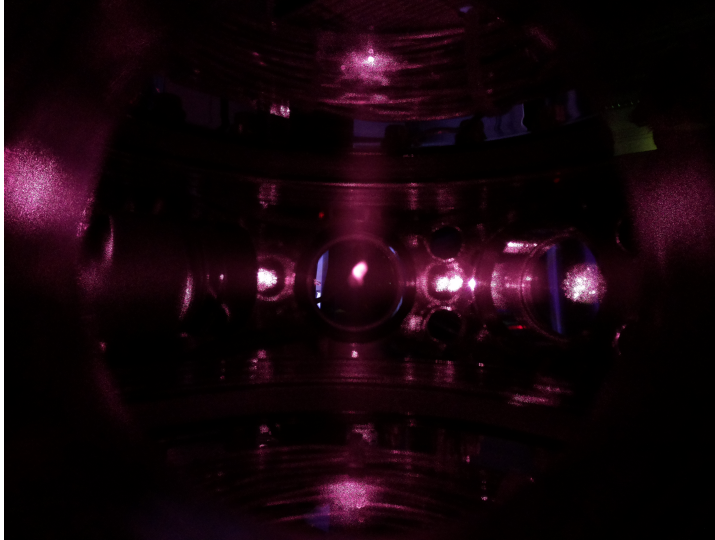
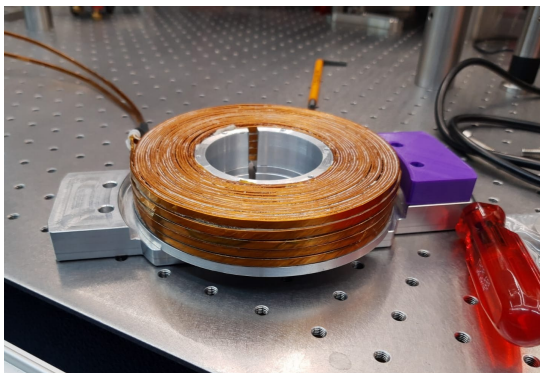


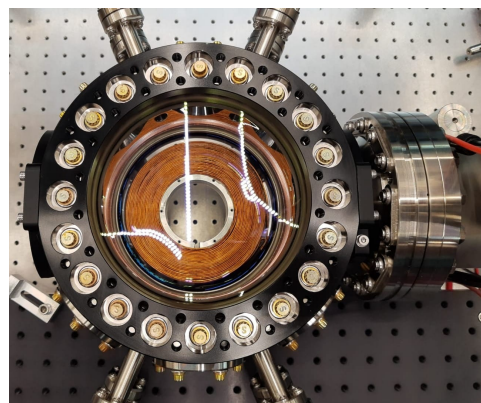
Figure 3.7: Photograph of the first  $^{87}\text{Rb}$  MOT made in the Laboratorio de Óptica Cuántica de Rydberg on november 24 2021.

### 3.2.2 Coils

To provide the magnetic field gradient in order to make a MOT we built two coils as depicted in figure 3.8. a total of 24 radial turns by 5 longitudinal turns of a copper wire with 0.4 cm of height and 0.1 cm of width delivers a gradient of  $2.29\ \text{G}/\text{Acm}^2$ . For the experiments reported in the next chapter we used 13.6 A yielding a total gradient of  $31.14\ \text{G}/\text{cm}^2$ .



(a)



(b)

Figure 3.8: Coils built for the magneto-optical trap of  $^{85}\text{Rb}$  and  $^{87}\text{Rb}$  atoms.

### 3.2.3 Optics

The laser beams of our MOT are in a free space configuration. This means three pairs of orthogonal counterpropagating laser beams with both the cooling and repumping beams intersect at the center of the science chamber. A total power of 150 mW of the cooling light and 15 mW of repumping light are divided in six branches. A photo of the optical arrangement around the science chamber is presented in figure 3.9.

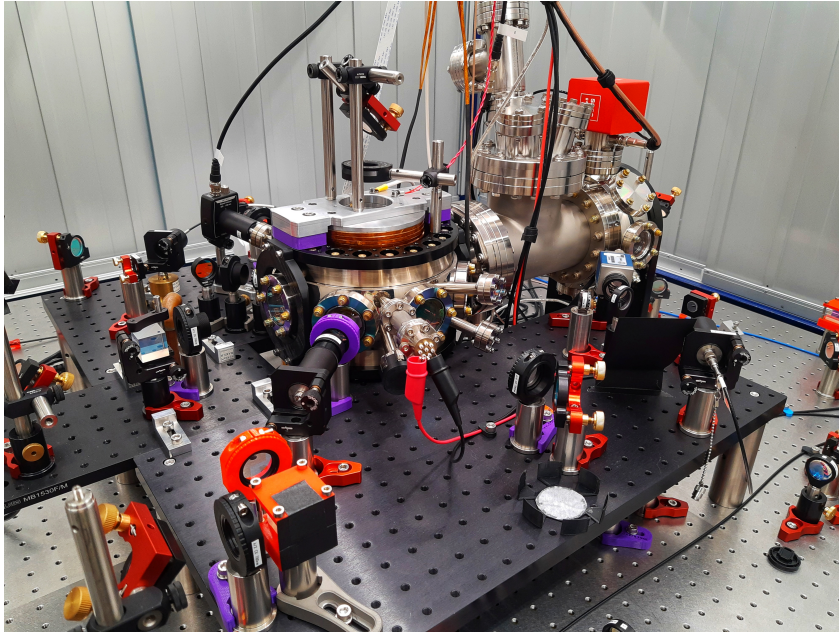


Figure 3.9: Photo of the science chamber and the optical arrangement we use for the MOT.

## 3.3 EIT with Rydberg states

Here we describe the experimental details for the observation of EIT with Rydberg states. The optics, experimental sequence for acquiring data, and data processing are described.

### 3.3.1 Optics

In order to produce the transparency window we excite the transition  $5S_{1/2} \rightarrow 5P_{3/2} \rightarrow 28S_{1/2}$  of  $^{87}\text{Rb}$  using two counterpropagating beams placed in a different axis from the MOT beams as depicted in figure 3.10. A focused probe beam with  $\sim 80 \mu\text{m}$  of waist is focused onto the cloud with a size of  $\sim 700 \mu\text{m}$  while the control beam is kept collimated with  $\sim 650 \mu\text{m}$  of waist.

We focus the probe beam in the cold gas with two purposes: focusing the beam allows us to pass all the light through the cloud and in this way we maximize the optical density, moreover

the focused probe beam has a smaller waist than the control beam taking advantage of all the control beam power to excite the atoms to Rydberg states. The powers of both beams vary from tens of  $\mu\text{W}$  to hundreds of mW, they are specified in the next chapter for each graph.

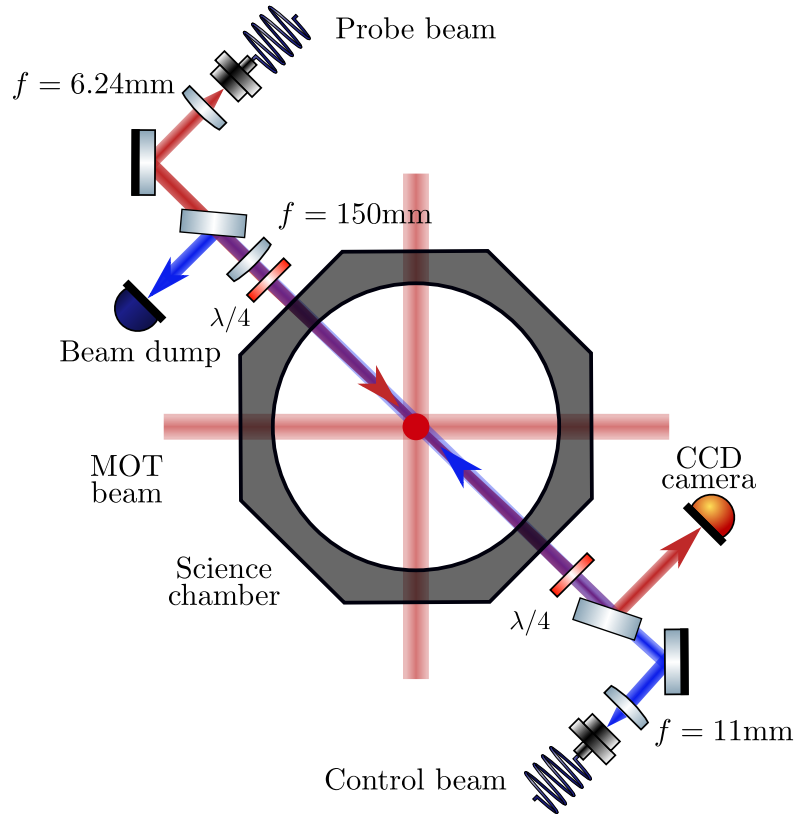


Figure 3.10: Optical scheme for the generation of Rydberg states under EIT conditions.

Both beams come from a single-mode polarization maintaining fiber, two quarter-wave plates allows us to change the polarization from linear to circular. The two fields must have a circular and opposite polarization as described in chapter 2. The same circular polarization won't excite the atom to Rydberg states as depicted on figures 2.2 and 2.5.

### 3.3.2 Sequence and data processing

Now we describe the experimental sequence we used for acquiring the data. First we load the MOT for 3 s, during this time we trap  $\sim 8 \times 10^{10}$  atoms of  $^{87}\text{Rb}$ . Then the MOT light is turned off by means of acousto optic modulators (AOM) and shutters installed in each branch of the secondary lasers, at the same time we shutdown the current passing through the coils, this only takes  $\sim 50 \mu\text{s}$ . We let the sample expand for 2.3 ms of time of flight and then we drive the probe beam with his frequency locked in a  $\delta_1$  value and control beam locked in  $\delta_2 = 0$  through the cloud and collect the probe beam with a CCD camera for  $200 \mu\text{s}$ , this is the “atom-



light photograph”. Then, we take two more photographs one just with the lasers on “light photograph” and one with everything off in the experiment called “darkness photograph”. This sequence is depicted in figure 3.11. For each value of  $\delta_1$  we want to measure a different MOT is loaded.

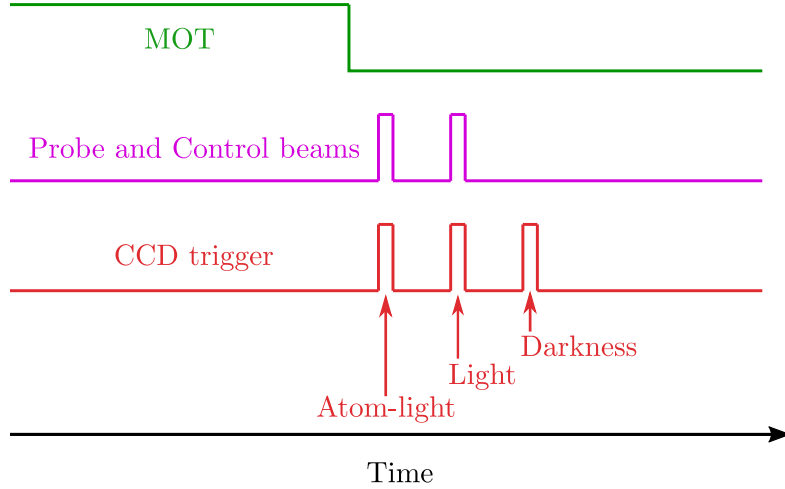


Figure 3.11: Experimental sequence used for the acquisition of data to detect EIT with Rydberg states in a  $^{87}\text{Rb}$  MOT. The loading time of the MOT is 3 s. Time of flight 2.3 ms. The exposure time of the CCD is  $200\ \mu\text{s}$ .

We use a homemade program for imaging analysis. The photographs of atom-light and light are cropped to a region of interest inside of the probe beam to maximize the signal to noise ratio. We calculate the integral of the region of interest for each of the images and we subtract the integral of the darkness photograph to each integral. Finally we divide this values to obtain the transmittance as:

$$T = \frac{\text{atom-light} - \text{darkness}}{\text{light} - \text{darkness}}. \quad (3.1)$$

As the locking point of the probe beam scans around the  $5S_{1/2}, F = 2 \rightarrow 5P_{3/2}, F' = 3$  transition the transmittance reveals the transparency window we are looking for.



# Chapter 4

---

---

## Results

---

---

4.1	EIT with Rydberg states . . . . .	37
4.1.1	Control frequency dependence . . . . .	39
4.1.2	Power dependence . . . . .	40
4.1.3	Polarization dependence . . . . .	42

In this chapter we present the experimental results. The measurements of electromagnetically induced transparency with Rydberg states are shown giving a discussion of our observations. We calculate fits for the measurements using the model developed in subsection 1.2.3. The powers of the probe and control beams are specified for each graph.

We measure the transmittance, see equation 3.1, with the control frequency fixed and probe frequency scanning around the  $5S_{1/2}, F = 2 \rightarrow 5P_{3/2}, F' = 3$  transition. For each experiment we took a higher density of points near the EIT window. To ensure us that no interesting structure was outside the EIT profile we made a measurement with a high density of points for all the  $\delta_p$  range but nothing was observed.

### 4.1 EIT with Rydberg states

First we observe what would happen with the control beam off ( $\Omega_c = 0$ ), this profile corresponds only to the  $5S_{1/2} \rightarrow 5P_{3/2}$  transition. Then we turned the control beam on ( $\Omega_c \neq 0$ ) and multiple windows of transparency were observed confirming the excitation to Rydberg states to  $n = 28$ , see figure 4.1.

As we are working with real atoms the hyperfine structure we discussed on chapter 1 is relevant, five hyperfine ground levels  $|g, m_F\rangle$  with  $F = 2$ , seven hyperfine first excited levels  $|e, m_F\rangle$  with  $F = 3$  and two fine Rydberg levels  $|r, m_J\rangle$  with  $J = 1/2$  giving a total of fourteen

levels are necessary to describe our system. Instead of observing only one transmission window we observe a set of windows with a variety of amplitudes. This means that the structure of the hyperfine levels reveals a set of windows for each possible transition. We developed a program to fit our data using what we described in subsection 1.2.3 depicted in figure 4.1 with a solid line.

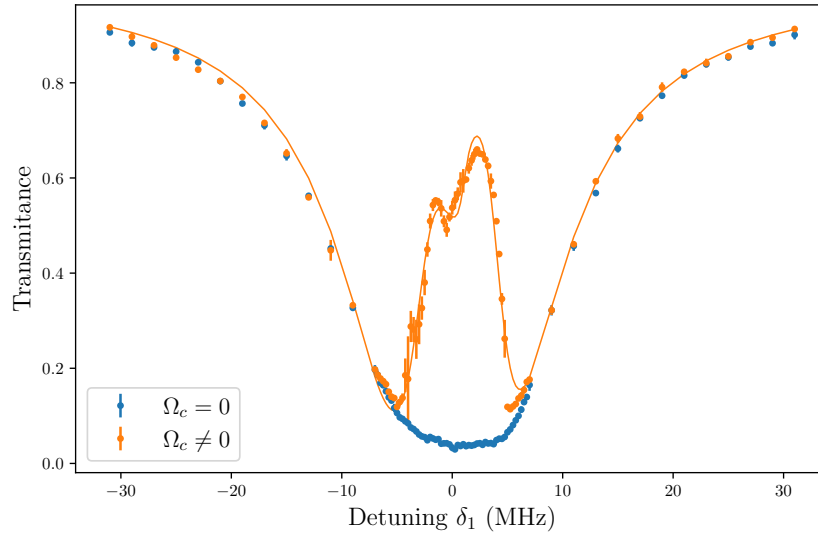


Figure 4.1: Transmittance profile of the atomic media as the probe beam is scanned around the  $5S_{1/2} \rightarrow 5P_{3/2}$  transition with control beam off (blue dots) and control beam on (orange dots). To make the fit shown with a solid line we constrain the polarization purities between 0.9 and 1.0 for each beam, the optical density on resonance  $OD_0 = 10$  as we can measure it when the control beam is off and we let the detuning  $\delta_2$  as well as the intensities of the probe and control beam  $I_p$  and  $I_c$  as free parameters. Multiple windows of transparency arise due to the hyperfine structure of the  $^{87}\text{Rb}$  atoms. Here we use a power of  $1.46 \mu\text{W}$  of the probe beam and  $55 \text{ mW}$  of control beam.

In this case to make the fit shown in figure 4.1 we constrain the polarization purities between 0.9 and 1.0, this is the fraction of the actual intensity that its been driven with  $\sigma_+$  and  $\sigma_-$  polarizations for the probe and control beams respectively, for each beam, the optical density on resonance  $OD_0 = 10$  as we can measure it when the control beam is off and we let the detuning  $\delta_2$  as well as the intensities of the probe and control beam  $I_p$  and  $I_c$  as free parameters. Although we can measure the power and estimate the waist of the beam the position of the waist lays inside of the science chamber and the alignment of the beams in reference to the atomic cloud is hard to be made with precision.

If we want to get rid of the multiple transparency windows and observe one we would have to build an effective three level system and there is a way to do it. Through optical pumping, in which we use beams with accurate polarization driving a non cycling transition,

we can drive the population to a well defined maximum or minimum of the quantum magnetic projection numbers  $m_F$ , in this case almost all atoms would be in states  $|g, -2\rangle$  or  $|g, 2\rangle$  to begin the excitation processes. As shown in figures 2.3, 2.2 and 2.5 if we start in state  $|g, 2\rangle$  and use  $\sigma_+$  polarization for the probe beam and  $\sigma_-$  for the control beam we get an effective dynamic of a three level atom, the same would happen with state  $|g, -2\rangle$  but with  $\sigma_-$  and  $\sigma_+$  polarizations respectively. Moreover, we need three pairs of coils, two for each orthogonal axis, that compensate the magnetic field of the earth. The combination of optical pumping and compensation fields would help us build an effective three level atom.

#### 4.1.1 Control frequency dependence

Next we explore how a change in the frequency of the control beam would change the EIT profile we observed before. To do this we change the locking point of the control laser  $-2$  MHz away from resonance and measure again the transmittance. As expected we observed that the whole set of transparency windows move together, see figure 4.2. This also rules out that the structure observed is due to CCD frequency dependent saturation effects.

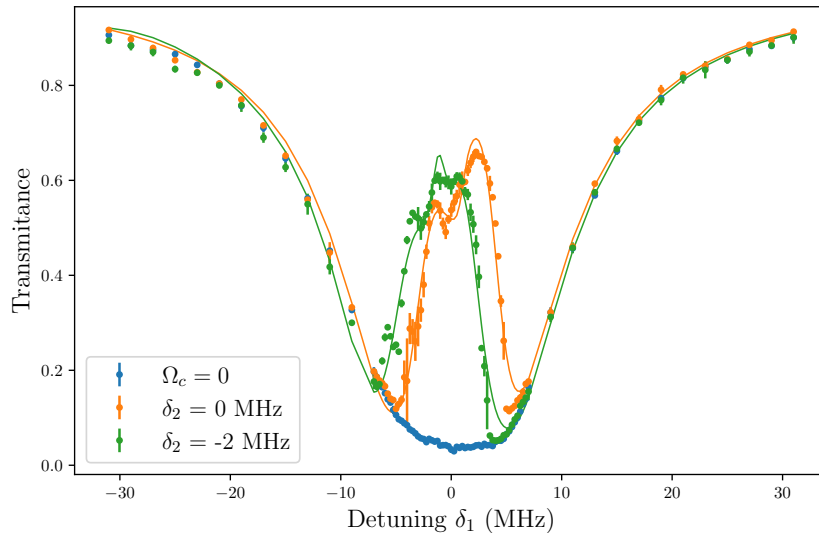


Figure 4.2: Transmittance profile of the atomic media with two different values of control beam detuning  $\delta_2 = 0$  MHz (orange dots) and  $\delta_2 = -2$  MHz (green dots), base line for reference (blue dots), the fits are shown with solid lines. To make the shifted window fit we constrain the polarization purities between 0.9 and 1.0 for each beam, the optical density on resonance  $OD_0 = 10$  and we let the detuning  $\delta_2$  as well as the intensities of the probe and control beam  $I_p$  and  $I_c$  as free parameters resulting in  $\delta_2 = -1.5320$  MHz. The set of EIT windows moves together as the frequency of the control beam changes. Here we use a power of  $1.46 \mu\text{W}$  of the probe beam and  $55 \text{ mW}$  of control beam.

To make the fit we constrain the polarization purities between 0.9 and 1.0 for each beam,

the optical density on resonance  $OD_0 = 10$  and we let the detuning  $\delta_2$  as well as the intensities of the probe and control beam  $I_p$  and  $I_c$  as free parameters. The fit reflects the change in control detuning as  $\delta_2$  is the only parameter different from the fit with  $\delta_2 = 0$  resulting in  $\delta_2 = -1.5320$  MHz.

### 4.1.2 Power dependence

One parameter we can change in both the probe and control beams is the power of the light. We performed two measures changing the power of one beam while the other was kept fixed.

First we leave the probe beam at  $1.46 \mu\text{W}$  while we change the control power output, the result is shown on figure 4.3. We observe that as the power increases some of the structure of the EIT windows vanishes as they start to combine with each other, but there still exist a set of transparencies we can identify. As the power decreases some transparencies vanish before others but in the end we keep three of them. Also an increasing power makes a wider set of windows.

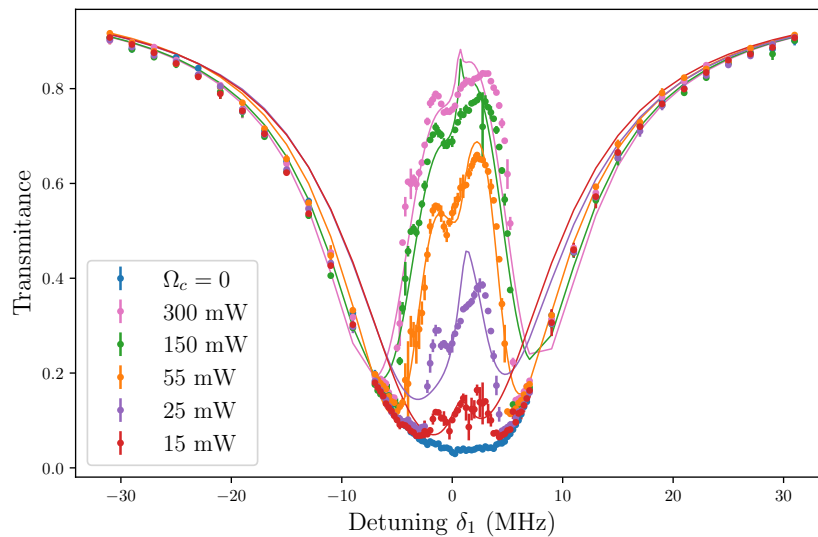


Figure 4.3: Transmittance profile of the atomic media for different control beam powers (dotted plots). The fits shown with solid lines were made fixing the polarization purities between 0.9 and 1.0 as well as the probe beam intensity with the value calculated by the program for the 55 mW measurement and leaving the magnetic field, detunings and control beam intensity as free parameters. The probe beam power was kept at  $1.46 \mu\text{W}$ . The jump downwards of the green graph corresponds with a point taken when control beam was unlocked from  $\delta_2 = 0$ .

The fits shown in figure 4.3 with solid lines were made fixing the polarization purities between 0.9 and 1.0 as well as the probe beam intensity with the value calculated by the program for the 55 mW measurement and leaving the magnetic field, detunings and control beam intensity

as free parameters. The fits correctly gives as the difference between each measurement the intensity of the control beam.

Then we proceeded with the power of the probe beam keeping the control power at 70 mW. As we can see in figure 4.4 when we increase the power all the structure of the transparencies vanishes and we observe a single wider EIT window as the transitions are saturated. When the power decreases the structure of the windows become clear and we can see three of them at the lowest power, same as when we decrease the control beam power.

The fits shown in figure 4.4 with solid lines were made fixing the polarization purities between 0.9 an 1.0 as well as the control beam intensity with the value calculated by the program for the  $1.56 \mu\text{W}$  measurement and leaving the magnetic field, detunings and probe beam intensity as free parameters. The fits correctly gives as the difference between each measurement the intensity of the probe beam.

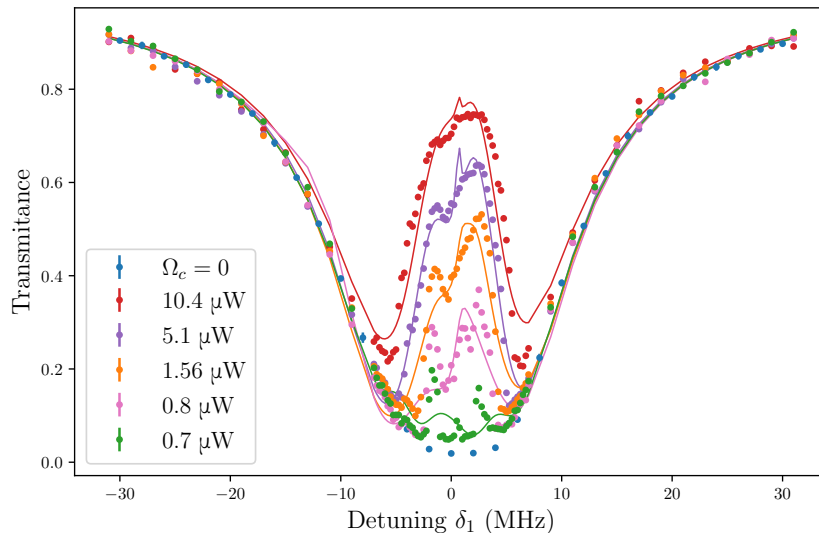


Figure 4.4: Transmittance profile of the atomic media for different probe beam power outputs (dotted plots). The fits are shown with solid lines these were made fixing the polarization purities between 0.9 an 1.0 as well as the control beam intensity with the value calculated by the program for the  $1.56 \mu\text{W}$  measurement and leaving the magnetic field, detunings and probe beam intensity as free parameters. The control beam power was kept at 70 mW.

Our first explanation for the multiple transparency windows was a Zeeman splitting but the results are consistent with a  $B = 0$  field. A possible explanation could be a differential light shift of each magnetic sublevel due to their different Clebsch-Gordan coefficients this is confirmed by observing that the width of the windows change as the probe power change.

One must notice that in order to saturate the transitions with control beam power it took hundreds of mW, while for the probe beam only took tens of  $\mu\text{W}$ . Moreover the fits for high control power are considerably better than the fits for the low power measurements. Right now

the model does not take into account inhomogeneous laser beams and atomic distributions. Moreover we need to improve the alignments of the beams to the atomic cloud to ensure that we are indeed focusing the probe beam onto the cloud.

### 4.1.3 Polarization dependence

Finally we rotated the quarter-wave plate of the control beam to change the polarization of the field from a circular polarization to the other circular polarization passing through elliptical and lineal polarizations on the way. As we described in chapter 2 if the polarization of the control beam is the same as the probe beam there should not be Rydberg excitations.

Using  $1.46 \mu\text{W}$  of the probe beam and  $55 \text{ mW}$  of control beam we measure the EIT window starting from the point of maximum transparency and rotated the quarter-wave plate each  $10^\circ$  degrees, the results are shown in figure 4.5.

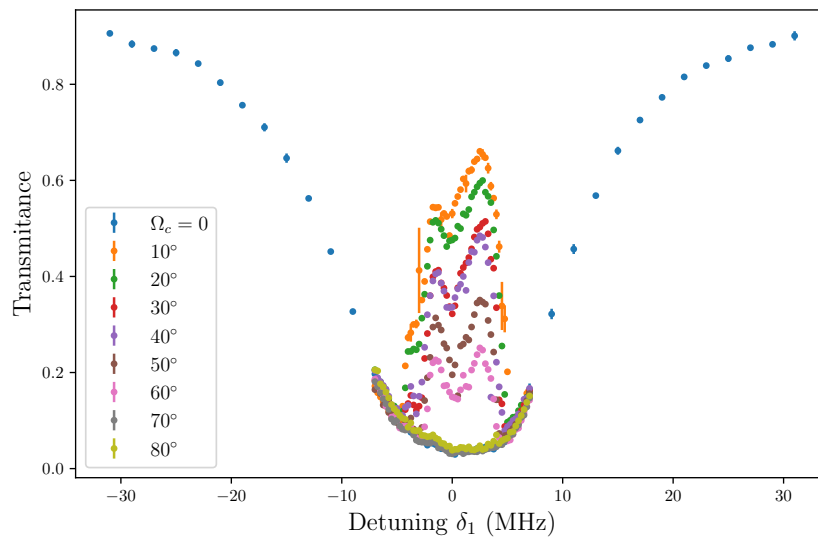


Figure 4.5: Transmittance profile of the atomic media as we rotate the control beam quarter-wave plate (dotted plots). We use  $1.46 \mu\text{W}$  of the probe beam and  $55 \text{ mW}$  of control beam for this measure.

We see that for the interval from  $70^\circ$  to  $80^\circ$  the EIT phenomenon disappears. Moreover, as we rotate the plate the structure of the EIT windows became more clear as some transitions cease to be excited. One transition to the far left stayed and was clear until the last angle in which we see EIT, this peak wasn't observable when we change the power of the beams. The width of the transparencies does not change as the plate was rotated. In this case no fit was implemented, the reason for not putting them is that in the model we made assumptions that are not fulfilled in the case of varying the polarization.



## Chapter 5

---

---

# Conclusions and perspectives

---

---

5.1	Conclusions . . . . .	43
5.2	Optical pumping and magnetic compensation fields . . . . .	44
5.3	Sub-Doppler cooling . . . . .	44
5.4	Observation of quantum nonlinearities . . . . .	45

Finally we give the conclusions of this work and talk about the pending works in the near future for the Laboratorio de Óptica Cuántica de Rydberg.

### 5.1 Conclusions

We developed a digital locking system using an all digital phase detection and beat frequency pre-scaling to phase lock the frequency differences between two lasers up to 7 GHz using their beatnote to generate the error signal. Two modulation techniques were implemented to lock the lasers, fast modulation of the diode current and slow modulation of the piezo-electric actuator that fine tune the output wavelength. Using this locking system we successfully locked the cooling, repumping and probe lasers to a primary laser locked to a high finesse cavity via the Pound-Drever-Hall technique. This system allowed us to generate the first  $^{87}\text{Rb}$  MOT in the Laboratorio de Óptica Cuántica de Rydberg.

We built an experiment to generate Rydberg excitations in a magneto-optical trap of  $^{85}\text{Rb}$  and  $^{87}\text{Rb}$  through the excitation path:

$$5S_{1/2} \rightarrow 5P_{3/2} \rightarrow nS/nD. \quad (5.1)$$

We used this system to excite a sample of  $\sim 10^8$  atoms of  $^{87}\text{Rb}$  at  $\sim 100\mu\text{K}$  to a  $28S$  Ryd-

berg level. We successfully detected the Rydberg excitations using electromagnetically induced transparency. The EIT profiles contain multiple windows of transparency due to the hyperfine structure of the atoms. We explained this set of EIT windows and provide a fit to the data.

## 5.2 Optical pumping and magnetic compensation fields

The next step in the construction of the laboratory is the implementation of a system that simplifies the excitation paths of the levels and allow us to have a fine control of the quantum states population. For this we have to implement an optical pumping and three pairs of magnetic compensation coils.

The optical pumping means using a specific frequency and polarization to drive the atoms in the MOT to a quantum state with a well defined quantum magnetic projection number. On the other hand the compensation coils are made in order to compensate for the magnetic field of the earth disabling the effect it has on the energy levels. A drawing of the coils is shown in figure 5.1

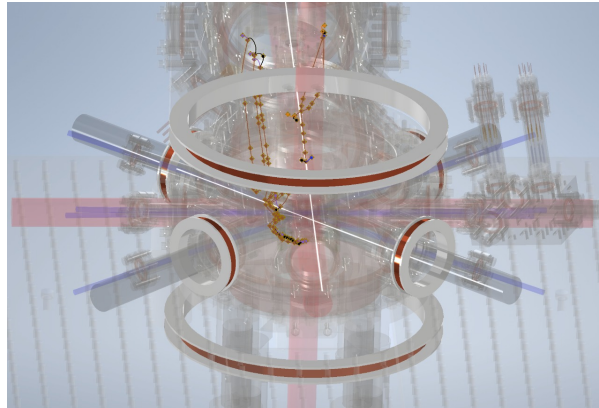


Figure 5.1: Drawing of the magnetic field compensation coils for the Laboratorio de Óptica Cuántica de Rydberg experiment.

## 5.3 Sub-Doppler cooling

Right now we use a magneto-optical trap to cool and contain the atoms but this technique has a limit, called the Doppler limit, on how much we can cool the sample and we have reached that point. To cool below this limit there are many methods and we want to explore the gray molasses [34] technique. Here we will use the dark states of the atoms to cool them down to  $4\mu\text{K}$ , unlike the MOT where we use bright states and only reach  $100\mu\text{K}$ . Cooling the sample below the Doppler limit will give us a better optical density and a better signal to noise ratio in the measurements.

## 5.4 Observation of quantum nonlinearities

As we described in chapter 1 the EIT phenomenon produces slowly propagating photons, if one couples them to highly excited Rydberg states quantum nonlinearities are obtained due to the Rydberg blockade effect. The quantum nonlinearity can be viewed as a photon–photon blockade mechanism that prevents the transmission of any multi-photon state. An experiment to produce this nonlinearities was performed for the first time by Peyronel *et al.* [12] with principal quantum numbers  $n = 100$ .

To this point we have achieved a medium that exhibits the EIT phenomenon in a cold atomic sample. Moreover, our laser system is designed to generate atoms in Rydberg states up to  $n \approx 120$  but if we want to achieve this Rydberg excitations an electric compensation field will be needed. We hope that in the near future we will be able to reproduce the results from Peyronel *et al.* [12] in the Laboratorio de Óptica Cuántica de Rydberg and measure the Wigner function of the light transmitted by this medium as this have not been characterized before.



---

---

# Bibliography

---

---

- [1] Ofer Firstenberg et al. “Attractive photons in a quantum nonlinear medium”. In: *Nature* 502.7469 (2013), pp. 71–75.
- [2] Daniel Tiarks et al. “Single-photon transistor using a Förster resonance”. In: *Physical Review Letters* 113.5 (2014), pp. 1–5.
- [3] W. Chen et al. “All-Optical Switch and Transistor Gated by One Stored Photon”. In: *Science* 341.6147 (Aug. 2013), pp. 768–770.
- [4] H. Gorniaczyk et al. “Single-photon transistor mediated by interstate Rydberg interactions”. In: *Physical Review Letters* 113.5 (2014), pp. 1–5.
- [5] O Firstenberg, C S Adams, and S Hofferberth. “Nonlinear quantum optics mediated by Rydberg interactions”. In: *Journal of Physics B: Atomic, Molecular and Optical Physics* 49.15 (2016), p. 152003.
- [6] K. M. Birnbaum et al. “Photon blockade in an optical cavity with one trapped atom”. In: *Nature* 436.7047 (2005), pp. 87–90.
- [7] E. Vetsch et al. “Optical interface created by laser-cooled atoms trapped in the evanescent field surrounding an optical nanofiber”. In: *Physical Review Letters* 104.20 (2010), pp. 1–4.
- [8] M. D. Lukin et al. “Dipole blockade and quantum information processing in mesoscopic atomic ensembles”. In: *Physical Review Letters* 87.3 (2001), pp. 37901–1–37901–4. DOI: 10.1103/PhysRevLett.87.037901.
- [9] Michael Fleischhauer and Jonathan P Marangos. “Electromagnetically induced transparency: Optics in coherent media”. In: *Reviews of Modern Physics* 77 (April 2005), pp. 633–673. ISSN: 0034-6861. DOI: 10.1103/RevModPhys.77.633.
- [10] A. K. Mohapatra, T. R. Jackson, and C. S. Adams. “Coherent optical detection of highly excited Rydberg states using electromagnetically induced transparency”. In: *Physical Review Letters* 98.11 (Mar. 2007), pp. 1–4.

- 
- [11] Y. O. Dudin and A. Kuzmich. “Strongly interacting Rydberg excitations of a cold atomic gas”. In: *Science* 336.6083 (2012), pp. 887–889.
- [12] Thibault Peyronel et al. “Quantum nonlinear optics with single photons enabled by strongly interacting atoms”. In: *Nature* 488.7409 (2012), pp. 57–60. DOI: 10.1038/nature11361.
- [13] D. Maxwell et al. “Storage and control of optical photons using Rydberg polaritons”. In: *Physical Review Letters* 110.10 (2013), pp. 1–5.
- [14] Daniel A. Steck. *Quantum and Atom Optics*. available online in <http://steck.us/teaching>, 2007, revision 0.12.6 from 23 of april 2019.
- [15] S E Harris, J E Field, and A K Edward. “Dispersive properties of electromagnetically induced transparency”. In: *Physical Review A* 46 (1992).
- [16] Marian O Scully. “Enhancement of the Index of Refraction via Quantum Coherence”. In: *Physical Review Letters* 67 (1991).
- [17] L. V. Hau et al. “Light speed reduction to 17 metres per second in an ultracold atomic gas”. In: *Nature* 397.February (1999), pp. 594–598.
- [18] Gianni Di Domenico, Stéphane Schilt, and Pierre Thomann. “Simple approach to the relation between laser frequency noise and laser line shape”. In: *Applied Optics* 49.25 (2010), p. 4801.
- [19] C.J. Foot. *Atomic Physics*. 1st ed. Oxford, 2005. ISBN: 0-19-850695-3.
- [20] J.J. Sakurai. *Modern Quantum Mechanics*. 1st ed. Addison-Wesley, 1994. ISBN: 0-201-53929-2.
- [21] Daniel A. Steck. *Rubidium 85 D Line Data*. disponible en línea en <http://steck.us/alkalidata>, 2019, revisión 2.2.1 del 21 de Noviembre 2019.
- [22] Daniel A. Steck. *Rubidium 87 D Line Data*. disponible en línea en <http://steck.us/alkalidata>, 2019, revisión 2.2.1 del 21 de Noviembre 2019.
- [23] P. van der Straten H. J. Metcalf. *Laser Cooling and Trapping*. 1st ed. Springer, 1999. ISBN: 978-0-387-98728-6.
- [24] J. D. Pritchard et al. “Cooperative atom-light interaction in a blockaded Rydberg ensemble”. In: *Physical Review Letters* 105 (19 Nov. 2010). ISSN: 00319007. DOI: 10.1103/PhysRevLett.105.193603.
- [25] Robert Löw et al. “An experimental and theoretical guide to strongly interacting Rydberg gases”. In: *Journal of Physics B: Atomic, Molecular and Optical Physics* 45.11 (2012).
- [26] Sebastian Weber et al. “Calculation of Rydberg interaction potentials”. In: *Journal of Physics B: Atomic, Molecular and Optical Physics* 50.13 (July 2017), p. 133001.

- 
- [27] T. F. Gallagher. *Rydberg Atoms*. 1st ed. Cambridge, 1994. ISBN: 0-521-38531-8.
- [28] Jun Ye et al. *Hyperfine structure and absolute frequency of the 87 Rb 5P 3/2 state*. 1996.
- [29] Eduardo Esquivel Ramírez. “Construcción de sistema de láseres para la generación de átomos de Rydberg”. Facultad de Ciencias, UNAM, Oct. 2020.
- [30] Eric D. Black. “An introduction to Pound–Drever–Hall laser frequency stabilization”. In: *American Journal of Physics* 69.1 (2002), pp. 79–87.
- [31] Jürgen Appel, Andrew MacRae, and A. I. Lvovsky. “A versatile digital GHz phase lock for external cavity diode lasers”. In: *Measurement Science and Technology* 20.5 (May 2009), p. 055302.
- [32] Martijn Jasperse. “Faraday Magnetic Resonance Imaging of Bose-Einstein Condensates”. PhD thesis. School of Physics and Astronomy, Monash University, Dec. 2015.
- [33] Edgar Giovanni Alonso Torres. “Diseño de sistema de vacío para experimentos de óptica cuántica con átomos de Rydberg”. Facultad de Ciencias, UNAM, Sept. 2020.
- [34] Sara Rosi et al. “ $\Lambda$ -enhanced grey molasses on the D 2 transition of Rubidium-87 atoms”. In: *Scientific Reports* 8 (1 2018), pp. 1–9. ISSN: 20452322. DOI: 10.1038/s41598-018-19814-z. URL: <http://dx.doi.org/10.1038/s41598-018-19814-z>.